

















This article has been accepted for publication in Monthly Notices of the Royal Astronomical Society ©: 2021 The Authors. Published by Oxford University Press on behalf of the Royal Astronomical Society. All rights reserved.

Spatially resolved star formation and inside-out quenching in the TNG50 simulation and 3D-HST observations

Erica J. Nelson ^{1,2}★, Sandro Tacchella ², Benedikt Diemer ³, Joel Leja ^{4,5,6}, Lars Hernquist,²
 Katherine E. Whitaker,^{7,8} Rainer Weinberger ², Annalisa Pillepich ⁹, Dylan Nelson ¹⁰,
 Bryan A. Terrazas ², Rebecca Nevin,² Gabriel B. Brammer,^{8,11} Blakesley Burkhart ^{12,13},
 Rachel K. Cochrane ², Pieter van Dokkum,¹⁴ Benjamin D. Johnson,² Federico Marinacci ¹⁵,
 Lamiya Mowla ¹⁶, Rüdiger Pakmor ¹⁸, Rosalind E. Skelton,¹⁷ Joshua Speagle,^{16,19} Volker Springel ¹⁸,
 Paul Torrey ²⁰, Mark Vogelsberger ²¹ and Stijn Wuyts²²

Affiliations are listed at the end of the paper

Accepted 2021 July 9. Received 2021 June 11; in original form 2021 February 5

ABSTRACT

We compare the star-forming main sequence (SFMS) of galaxies – both integrated and resolved on 1 kpc scales – between the high-resolution TNG50 simulation of IllustrisTNG and observations from the 3D-HST slitless spectroscopic survey at $z \sim 1$. Contrasting integrated star formation rates (SFRs), we find that the slope and normalization of the star-forming main sequence in TNG50 are quantitatively consistent with values derived by fitting observations from 3D-HST with the `Prospector` Bayesian inference framework. The previous offsets of 0.2–1 dex between observed and simulated main-sequence normalizations are resolved when using the updated masses and SFRs from `Prospector`. The scatter is generically smaller in TNG50 than in 3D-HST for more massive galaxies with $M_* > 10^{10} M_\odot$, by ~ 10 –40 per cent, after accounting for observational uncertainties. When comparing resolved star formation, we also find good agreement between TNG50 and 3D-HST: average specific star formation rate (sSFR) radial profiles of galaxies at all masses and radii below, on, and above the SFMS are similar in both normalization and *shape*. Most noteworthy, massive galaxies with $M_* > 10^{10.5} M_\odot$, which have fallen below the SFMS due to ongoing quenching, exhibit a clear central SFR suppression, in both TNG50 and 3D-HST. In contrast, the original Illustris simulation and a variant TNG run without black hole kinetic wind feedback, do not reproduce the central SFR profile suppression seen in data. In TNG, inside-out quenching is due to the supermassive black hole (SMBH) feedback model operating at low accretion rates.

Key words: galaxies: evolution – galaxies: formation – galaxies: high-redshift – galaxies: star formation – galaxies: structure.

1 INTRODUCTION

Very generally, the fundamental challenge in trying to understand how galaxies form is that it happens over such long time-scales. At its present star formation rate, the Milky Way would take over thirty billion years to double its stellar mass (e.g. Licquia & Newman 2015). No matter the advances in telescope technology, we cannot watch a galaxy through the billions of years of its evolution to see how it builds its bulge and disc, what drives changes in its star formation rate, or how it responds to interactions with other galaxies or changes in accretion rate. Various methods have been devised to trace galaxies across cosmic time (e.g. van Dokkum et al. 2010; Behroozi, Wechsler & Conroy 2013; Leja et al. 2013; Moster, Naab & White 2013; Papovich et al. 2015; Torrey et al. 2017; Wellons & Torrey 2017). But clever as these methods are, they can only tell us about the statistical evolution of a population; they can give us a description of the buildup of a group of similar mass galaxies through time but cannot tell us how it happened. Additionally, the archaeological approach to galaxy

evolution tends to be mainly limited to understanding the stellar-mass assembly and chemical evolution of galaxies (e.g. Thomas, Greggio & Bender 1999; Graves, Faber & Schiavon 2009; Trager & Somerville 2009; Pacifici et al. 2016).

A complementary approach to this problem is to simulate galaxy formation rather than observe it. Simulating a universe in a box allows us to track galaxies through time to see how they grow and determine the key physical processes driving that growth. Cosmological hydrodynamical simulations evolve a box of dark matter, gas, stars, and supermassive black holes through time using gravity and hydrodynamics. Refining these simulations has informed us about the plethora of physical processes involved in galaxy formation. However, it is only in the last decade that hydrodynamical simulations have begun to produce galaxies with realistic morphologies (e.g. Governato et al. 2010; Brooks et al. 2011; Guedes et al. 2011; Aumer & White 2013; Ceverino et al. 2014; Christensen et al. 2014; Genel et al. 2014; Hopkins et al. 2014; Vogelsberger et al. 2014a, b; Crain et al. 2015; Khandai et al. 2015; Schaye et al. 2015; Sijacki et al. 2015; Zolotov et al. 2015; Davé, Thompson & Hopkins 2016; Dubois et al. 2016).

In general, these simulations come in two types: cosmological volumes focusing on population statistics at the expense of res-

* E-mail: erica.june.nelson@colorado.edu

olution, and zoom-in simulations focusing on individual galaxies at the expense of population statistics. With gradual improvements in physical models, computational methods, and spatial resolution, it has become possible to simulate a cosmological volume with resolution sufficient to study the structural evolution of galaxies (thousands of galaxies at sub-kpc resolution). TNG50 is the highest resolution simulation of the IllustrisTNG project, covering a 50 Mpc box with a median spatial resolution of ~ 100 pc (TNG: Weinberger et al. 2017; Marinacci et al. 2018; Naiman et al. 2018; Pillepich et al. 2018; Springel et al. 2018; Nelson et al. 2018, 2019a, TNG50: Pillepich et al. 2019; Nelson et al. 2019b). Studying the structural evolution of galaxies and its relation to the regulation of star formation requires both the spatial resolution and the population statistics afforded by TNG50. However, before it is used for this purpose, the simulation needs to be validated against key observables.

In the space of colour and magnitude, we have long known that galaxies occupy the ‘blue cloud’ and ‘red sequence’ (e.g. Strateva et al. 2001; Blanton et al. 2003; Kauffmann et al. 2003; Bell et al. 2004; Faber et al. 2007; Brammer et al. 2009; Whitaker et al. 2011; Taylor et al. 2015). With improvements in our ability to constrain the physical properties of galaxies, we have found that this blue ‘cloud’ in colour–magnitude space resolves itself into a ‘sequence’ in SFR– M_* space. This so-called ‘star-forming main sequence’ (SFMS) is a somewhat sublinear relation between $\log(\text{SFR})$ and $\log(M_*)$. The normalization declines with time reflecting slower relative growth rates of galaxies through cosmic time (e.g. Daddi et al. 2007; Noeske et al. 2007; Salim et al. 2007; Karim et al. 2011; Rodighiero et al. 2011; Wuyts et al. 2011; Whitaker et al. 2012, 2014; Speagle et al. 2014; Schreiber et al. 2015; Shivaei et al. 2015; Tasca et al. 2015; Tomczak et al. 2016; Lee et al. 2018).

The star-forming main sequence has a 1σ scatter in SFR at fixed stellar mass of about a factor of 2 (Whitaker et al. 2012; Speagle et al. 2014) (which has been deemed ‘tight’). However, not all galaxies reside on the main sequence at all times, they form stars more rapidly or slowly over the course of their assembly history. What drives their evolution through this plane, however, remains uncertain. Star formation across the main sequence has been proposed to be regulated by mergers; episodes of ‘compaction’ and inside-out quenching; bursty star formation; self regulation by accretion and outflows; and variations in dark matter halo formation times (e.g. Hernquist 1989; Wuyts et al. 2011; Dekel et al. 2013; Sparre et al. 2015, 2017; Nelson et al. 2016; Tacchella et al. 2016a; Orr et al. 2017; Matthee & Schaye 2019; Tacchella, Forbes & Caplar 2020).

Recently, we have developed the ability to place spatially resolved constraints on the star-forming main sequence. This became possible owing to the capability of mapping tracers of star formation and stellar mass in representative samples of galaxies with e.g. *HST*/WFC3, VLT/SINFONI, SDSS IV/MAANGA, and in particular of measuring where star formation happens in galaxies on, above, and below the star-forming main sequence at different masses (Nelson et al. 2016; Abdurro’uf & Akiyama 2018; Belfiore et al. 2018; Ellison et al. 2018; Tacchella et al. 2018; Morselli et al. 2019). This tells us where star formation occurs when galaxies are forming stars normally and where it is enhanced and suppressed relative to the existing stars. Galaxy structure (such as radii and bulge fraction) and the regulation of star formation appear to be intimately coupled and this measurement provides a direct link between them.

The star-forming main sequence and spatially resolved patterns of star formation across it depend on several key aspects of galaxy formation models: where gas settles in galaxies, feedback, and the conversion of gas into stars. For this reason, the star-forming main sequence has been used regularly to validate simulations (e.g. Torrey

et al. 2014; Schaye et al. 2015; Somerville & Davé 2015; Sparre et al. 2015; Davé et al. 2016; Tacchella et al. 2016a; Donnari et al. 2019). However, while the star-forming main sequence in recent state-of-the-art simulations has been found to match observations qualitatively, it does not usually match quantitatively, typically having a normalization which is 0.1–1 dex too low especially at $z = 1–3$ (Somerville & Davé 2015). Specifically compared to the chosen observations in each work, it is 0.1–0.5 dex lower in Illustris at $1 < z < 2$ (Torrey et al. 2014; Sparre et al. 2015), 0.2 dex lower in EAGLE at $0.05 < z < 0.3$ (Schaye et al. 2015), 0.2–1 dex lower in SIMBA (Davé et al. 2019), and 0.2–0.5 dex lower in TNG100 (Donnari et al. 2019). This is also found based on mass conservation arguments in toy models (e.g. Dekel & Mandelker 2014; Leja et al. 2015).

It was unclear whether this was due to problems with the simulations or systematic uncertainties in the observations. Given the phenomenological nature of prescriptions for AGN and stellar feedback and star formation, it is entirely possible that this points to a problem with the simulations. On the other hand, measurements of star formation rates from observations are notoriously difficult and are typically subject to a factor of two systematic uncertainty. The other dimension of the SFR– M_* plane, stellar mass, is better constrained but still has systematic uncertainties of at least 0.1 dex (e.g. Muzzin et al. 2009). Resolved measurements of star formation across the main sequence have also been compared between observations and simulations yielding qualitative disagreements. While observations generally find specific star formation rate (sSFR) profiles that are flat or rising on and below the star-forming main sequence respectively, simulations typically find they are falling with radius, in particular below the main sequence and in sharp contrast to observations (FIRE, Illustris, SIMBA, respectively: Orr et al. 2017; Starkenburg, Tonnesen & Kopenhafer 2019; Appleby et al. 2020), although VELA provides a contrast (Tacchella et al. 2016b). In order to use a simulation to understand the structural evolution of galaxies and the regulation of star formation, we must be confident it reproduces the integrated star-forming main sequence and specific star formation rate profiles of galaxies across it. Understanding where the simulation can or cannot reproduce these key observables and determining why aids our physical interpretation of the observations based on the models we compare them with.

With high quality observational measurements and simulations with improved resolution and prescriptions for feedback, in this paper we compare the integrated star-forming main sequence and specific star formation rate radial profiles from the TNG50 magneto-hydrodynamical cosmological simulation, part of the IllustrisTNG suite, to that inferred from observations as part of the 3D-HST survey at $z \sim 1$. We first compare the normalization, slope, and scatter of the integrated star-forming main sequence. We then compare the resolved specific star formation rate radial profiles of galaxies below, on, and above the main sequence.

Hubble, *Spitzer*, and *Herschel* have spent thousands of hours imaging the CANDELS/3D-HST extragalactic legacy fields to place the best possible photometric constraints on the UV-FIR spectral energy distributions (SEDs) of galaxies which we model to derive physical parameters. This community investment provides the backbone of this work. Two additional features make our work unique. First, owing to the new Bayesian inference framework *Prospector*, we now have improved measurements of the star formation rates and stellar masses of galaxies changing observed estimates of the star-forming main sequence (Johnson & Leja 2017; Leja et al. 2017, 2019; Johnson et al. 2020). Secondly, owing to the *Hubble Space Telescope* (*HST*) WFC3/G141 grism and multiband imaging, we now have

spatially resolved measurements of the specific star formation rates for large samples of galaxies across the star forming main sequence (e.g. Nelson et al. 2016).

The observations on which this comparison is based are from the 3D-HST survey. The 3D-HST survey is a 248 orbit survey with the *HST* Wide Field Camera 3 (WFC3) grism which provided spatially resolved near-infrared spectra for 200 000 objects in the five major extragalactic legacy fields (Brammer et al. 2012a; Skelton et al. 2014; Momcheva et al. 2015). At $0.7 < z < 1.5$ these spectra can be used to create $H\alpha$ emission line maps, which trace where star formation is occurring (e.g. van Dokkum et al. 2011; Nelson et al. 2012, 2013; Brammer et al. 2012b; Lundgren et al. 2012; Schmidt et al. 2013; Wuyts et al. 2013; Vulcani et al. 2015, 2016), for 3200 galaxies with $9 < \log(M_*) < 11$ across the star-forming main sequence (e.g. Nelson et al. 2016), over an order of magnitude more than was previously possible. Enormous gains were made in our ability to map $H\alpha$ emission with near-infrared integral field units on 10-m class telescopes with adaptive optics (e.g. Förster Schreiber et al. 2006, 2009, 2011a, b; Tacchella et al. 2015b). The information content in these deep spectra allows detailed study of physical processes in those objects similarly to cosmological zoom simulations. As with the computational cost of zoom simulations, the observational costs of these types of observations are high, limiting the statistics to of the order of ~ 100 galaxies. The WFC3/G141 grism provided another window into this problem that is well matched to cosmological simulations like TNG. The slitless spectra provide spatially resolved emission line diagnostics for all objects in its field of view, dramatically increasing the multiplexing capabilities. On a strategic level, we note that with a richer information content, these VLT/SINFONI observations for tens of galaxies are well-matched to zoom simulations while *HST*/WFC3 grism observations are well-matched to simulations of cosmological volumes with thousands of galaxies. With a similar resolution and volume, TNG50 and 3D-HST are particularly well-suited to each other.

This paper is organized as follows. In Section 2, we describe the data used for this project and how we infer physical properties of galaxies from them. In Section 3, we describe the TNG50 simulation. In Section 4, we compare the integrated star-forming main sequence slope, normalization, and scatter in TNG50 to observations from 3D-HST/Prospector. In Section 5, we compare the specific star formation rate profiles of galaxies below, on, and above the star-forming main sequence between TNG50 and 3D-HST. In Section 6, we summarize our findings.

2 OBSERVATIONAL DATA

2.1 Integrated quantities

In this paper, the key quantities are redshifts, stellar masses, and star formation rates, both integrated and resolved in the case of the latter two. The 3D-HST+CANDELS data set is particularly well designed for deriving these quantities in the $z = 0.5\text{--}2$ Universe as it has 1 kpc spatial resolution imaging and spectroscopy in the rest-frame optical that is key for inferring structural stellar population properties. CANDELS is a 902 orbit *HST* survey providing optical and near-infrared imaging (Grogin et al. 2011; Koekemoer et al. 2011). 3D-HST is a 248 orbit *HST* survey including near-infrared imaging and slitless spectroscopy over the same area (van Dokkum et al. 2011; Brammer et al. 2012a; Skelton et al. 2014; Momcheva et al.

2016).¹ These surveys cover five major extragalactic fields AEGIS, COSMOS, GOODS-N, GOODS-S, and UDS which, crucially, have a wealth of publicly available data from the ultraviolet through the infrared (see table 3 of Skelton et al. 2014, for additional references Giavalisco et al. 2004; Grogin et al. 2011; Koekemoer et al. 2011; Whitaker et al. 2011, 2019; Brammer et al. 2012a; Ashby et al. 2013; Skelton et al. 2014; Momcheva et al. 2016; Oesch et al. 2018).

Redshifts are derived from template fits to the combination of photometry and near-infrared slitless spectroscopy (Momcheva et al. 2016). Galaxy stellar masses and star formation rates are derived by modeling the $0.3\text{--}24\ \mu\text{m}$ (UV-IR) spectral energy distribution (SED) from the observed photometry. Aperture photometry was performed on PSF-matched images to measure consistent colours across passbands. For the *HST* imaging, a $0''.7$ diameter aperture was used and an aperture correction was performed to arrive at the total flux (see Skelton et al. 2014, for many more details). To determine stellar population parameters, the SED is fit using the Bayesian inference framework Prospector (Johnson & Leja 2017) as presented in Leja et al. (2019). Prospector uses the Flexible Stellar Population Synthesis code (FSPS; Conroy & Wechsler 2009) to construct a physical model and the nested sampler dynesty to sample the posterior space (Speagle 2020). This model includes a non-parametric star formation history, a two-component dust attenuation model with a flexible attenuation curve, variable stellar metallicity, and dust emission powered by energy balance (see Leja et al. 2017, for more details). With this new model, our new catalogues have systematically higher stellar masses and lower star formation rates than previous versions (Leja et al. 2019). In this work, we use the SFRs averaged over the last 30 Myr.

2.2 Mapping stellar mass and star formation

In this paper, we compare specific star formation rate profiles of galaxies across the star-forming main sequence from TNG50 to observations at $z \sim 1$. Deriving specific star formation profiles observationally is challenging due primarily to the difficulty of mapping star formation. Our process for deriving sSFR profiles for this comparison builds on Nelson et al. (2016), so we refer the reader there for details. The primary update is that we use spatially resolved SED fitting to derive stellar mass maps and perform a dust correction to the $H\alpha$ emission to map star formation. We summarize our methodological choices and their impact below and briefly describe the rest of the analysis and the data from whence it came, with an emphasis on what is new and what is certain or uncertain.

Our aspiration here is to compare sSFR profiles from TNG50 to the real Universe, meaning that we need to map stellar mass and SFRs from observations. We map stellar mass and star formation in two ways, with one method closer to the data and the other with more layers of interpretation. In both of these analysis tracks we stack maps, correct for the effects of the point spread function (PSF) on the stack, and then construct radial surface brightness profiles. In the following section, we first describe the different ways we map sSFR and then describe the stacking, PSF-correcting, and profile extraction.

¹The 3D-HST data set is publicly available at <https://archive.stsci.edu/prepds/3d-hst/>

2.2.1 Resolved sSFR from maps of $H\alpha$ equivalent width

The method closest to the data is to simply use maps of $H\alpha$ equivalent width as a proxy for sSFR. Hot young stars photoionize their surrounding gas. The recombination and subsequent cascade of electrons in hydrogen atoms produces the $H\alpha$ [6563 Å] emission line (amongst others) which is thus a tracer of stars formed in the past ~ 10 million years. At the same wavelength, the rest-frame R -band continuum, light from the longer lived, lower mass stars that make up the bulk of the stellar mass become more important, making it an oft-used tracer of the distribution of stellar mass (e.g. van der Wel et al. 2014). Here, we trace this redshifted R -band emission with the WFC3/ JH_{F140} filter. The quotient of these, $H\alpha/JH_{F140}$, which we will here call the $H\alpha$ equivalent width ($EW(H\alpha)$) hence traces sSFR.

The key innovation here is the ability to map the $H\alpha$ emission line, a tracer of star formation, in large samples of galaxies. We do this using the slitless spectroscopy from the 3D-HST survey which provides spatially resolved maps of emission lines for everything in its field of view (e.g. Brammer et al. 2012b; Nelson et al. 2012, 2013, 2016; Lundgren et al. 2012; Schmidt et al. 2013; Wuyts et al. 2013; Vulcani et al. 2015, 2016). Due to its large multiplexing capacity and unbiased sampling, this mode has grown increasingly popular on *HST* and likely will on JWST as well. The grism (a portmanteau of ‘grating’ and ‘prism’), is a spectral element in the WFC3 IR channel filter wheel dispersing incident light on to the WFC3 detector, and as such providing spectra for all objects in the field of view. This observing mode features a unique combination of *HST*’s high native spatial resolution and the grism’s low spectral resolution: ~ 1 kpc and ~ 1000 km s $^{-1}$ at $z = 1$, our redshift of interest. This means that for all galaxies in our sample we will get a map of the spatial distribution of line-emitting gas. Because of the low spectral resolution, these spectra contain virtually no kinematic information; besides e.g. > 1000 km s $^{-1}$ outflows, the entire velocity structure of the galaxy will be contained in a single spectral resolution element. Hence, we obtain maps of the emission lines of all galaxies in the field of view which are redshifted into the wavelength coverage of the grism.

The wavelength coverage of the G141 grism (1.15–1.65 μ m) samples redshifted $H\alpha$ at $0.7 < z < 1.5$. The spectra of all objects in the field are forward modelled based on imaging. This provides the extraction window for each spectrum based on the geometric transformation on to the detector. Furthermore, because there is nothing blocking the light from other objects, many of the spectra overlap or ‘contaminate’ one another. The forward modelling also maps where contaminating flux from other objects will fall on the 2D spectrum of the object of interest. All pixels predicted to have contaminating flux more than a third of the background are masked. Finally, the continuum light of a galaxy is modelled by convolving the best-fitting SED without emission lines with its *HST* image at the same wavelength (combined $J_{F125W}/JH_{F140W}/H_{F160W}$). We subtract the continuum model from the 2D grism spectrum which simultaneously removes the continuum emission and corrects the $H\alpha$ maps for underlying stellar absorption. What remains for all 3200 galaxies at $0.7 < z < 1.5$ is a map of their $H\alpha$ emission. One complication of the low spectral resolution is that N II and $H\alpha$ are blended and S II and $H\alpha$ are separated by three resolution elements. To mitigate this, we use a double wedge mask along the dispersion direction covering S II. The overall contribution of N II has less of an impact because the total map is scaled to the integrated SFR measured from *Prospector* and the mask decreases the impact of very high ratios extending emission in the dispersion direction.

Radial gradients in N II/ $H\alpha$, on the other hand do matter. We account for these in Section 2.4.

More details on the reduction and analysis of the 3D-HST grism spectroscopy are available in Brammer et al. (2012a) and Momcheva et al. (2016); more details on the creation of $H\alpha$ maps are in Nelson et al. (2016). Mapping the JH_{F140} emission is much more straightforward. Stamps are cut around the objects in the interlaced frames. Light from nearby objects is masked according to the *SEXTRACTOR* segmentation map.

This first method for mapping sSFR comes straight from the data: it is simply the quotient of the measured $H\alpha$ map and the measured JH_{F140} map. No dust correction is done to either the $H\alpha$ or the JH_{F140} maps, with the assumption that they are subject to similar dust attenuation because they are at the same wavelength (modulo differential extinction toward H II regions) hence the dust attenuation multiplier cancels out in the quotient.

2.2.2 Resolved sSFR from spatially resolved SED fitting

The effect of dust attenuation in principle cancels when scaling the observed $H\alpha/JH_{F140}$ directly to sSFR (as described in the previous section). However, in addition to dust, the continuum light, which we are scaling to stellar mass, is also subject to age gradients which affect the mass-to-light ratio (M/L). In particular, the centres of galaxies are typically observed to be older than their outskirts (e.g. Wuyts et al. 2012; Cibinel et al. 2015; Tacchella et al. 2015a). Older stars have a higher M/L meaning that the stellar mass is more concentrated than the light. Consequently, the actual sSFR profiles could be more centrally depressed than the observed profiles of $H\alpha/JH_{F140}$.

Our second method attempts to mitigate the effects of dust and stellar age on the observed light using spatially resolved spectral energy distribution (SED) modelling to map the stellar mass and dust attenuation in our galaxies. Spatially resolved SED modelling is done using the eight band *HST* imaging described in Section 2.1. This methodology is described in detail in Cibinel et al. (2015), but we outline it here for completeness. Image postage stamps are cut from the mosaics in each *HST* band convolved by PSF-matching to the resolution of the reddest band, H_{F160} , which has the lowest resolution. The images are adaptively smoothed using *AdaptSmooth* (Zibetti, Charlot & Rix 2009) requiring $S/N > 5$ in each spatial bin in the H_{F160W} image, which has the highest S/N. The SPS code *LePhare* (Arnouts et al. 1999; Ilbert et al. 2006) is run on the photometry in each spatial bin using the Bruzual & Charlot (2003) synthetic spectral library, a Chabrier (2003) initial mass function, a Calzetti et al. (2000) dust law and three metallicity values ($Z = 0.2, 0.4, 1 Z_{\odot}$). The star formation history is parametrized as a delayed exponential (t/τ^2) exp ($-t/\tau$) having a characteristic time-scale τ with 22 values between 0.01 and 10 Gyr and a minimum age of 100 Myr.

We use the model $E(B - V)$ maps to correct our $H\alpha$ maps for the effects of dust using

$$A_{\text{cont}} = k(\lambda)E(B - V)$$

$$A_{\text{extra}} = 0.9A_{\text{cont}} - 0.15A_{\text{cont}}^2$$

$$F(H\alpha)_{\text{intr}} = F(H\alpha)_{\text{obs}} \times 10^{0.4A_{\text{cont}}} \times 10^{0.4A_{\text{extra}}},$$

where A_{cont} is the dust attenuation towards the stellar continuum at the wavelength of $H\alpha$. $k(\lambda)$ is computed using the Calzetti et al. (2000) dust attenuation law $k(H\alpha = 6563 \text{ \AA}) = 3.32$. A_{extra} is the amount of extra attenuation towards H II regions calculated using Wuyts et al. (2013). These dust corrected maps of SFR($H\alpha$) are then

divided by then the SED-modelled stellar mass to get the sSFR. Both are scaled to the integrated values from `Prospector`.

2.3 Selection

We select galaxies in the redshift range $0.75 < z < 1.5$ for which we can map the $H\alpha$ emission line using the *HST*/G141 grism. We confine this analysis to the mass range $9 < \log(M_*) < 11$; the lower boundary is driven by our completeness limit (Tal et al. 2014), the upper by number statistics. Here and for the remainder of this paper when we refer to $\log(M_*)$, it is in units of M_\odot . Here, we are interested in an analysis of the SFMS rather than the star formation properties of the full population of galaxies, so we select only those galaxies which are actively forming stars. We do this according to a doubling time criteria, specifically by comparing the doubling time to the age of the Universe (Tacchella et al. 2019). We use a slightly less restrictive criteria to encompass the tail of the distribution to low SFRs:

$$t_{\text{double}} < 20t_{\text{Hubble}}(z).$$

This corresponds to a galaxy’s current star formation rate doubling its mass in 20 Hubble times (or adding 5 per cent to its mass in a Hubble time). This is the extent of the selection criteria applied for Section 4 comparing the integrated SFMS in observations and TNG50.

For Section 5 comparing sSFR profiles across the main sequence, a few additional selection criteria are required on the observational side. We remove all galaxies flagged as having unreliable photometry as well as galaxies with X-ray luminosity $L_x > 10^{42.5} \text{erg s}^{-1}$ or $H\alpha$ emission line widths of $\sigma > 2000 \text{km s}^{-1}$ likely indicating that emission from an active galactic nucleus (AGN) will contaminate the central $H\alpha$ flux we interpret as star formation. For the $H\alpha$ maps, we also reject galaxies whose spectra are too badly contaminated (see Section 2.2.1). Together these criteria result in a selection of ~ 3200 galaxies. Finally, we note that we have maps of $E(B - V)$ in only two of our five fields, GOODS-N and GOODS-S, where there the HDUV program provides UV data.

2.4 Stacking and specific star formation rate profiles

We stack galaxies across the main sequence in bins of stellar mass and position with respect to the SFMS (ΔMS). Stellar mass bins are 0.5 dex from $\log(M/M_\odot) = 9-11$. We fit the SFMS as described in Section 4 and divide the galaxies into bins below, on, and above the main sequence according to $\log(\Delta\text{MS})$ $[-0.8, -0.4]$, $[-0.4, 0.4]$, and $[0.4, 1.2]$, respectively. The main sequence has a logarithmic scatter of ~ 0.3 dex, so our stacks of galaxies ‘on’ the main sequence include slightly more than those within $1 - \sigma$. As described in Nelson et al. (2016), this is done so that the bins above and below the main sequence would probe the top and bottom 10 per cent of star formers. To create each stack, we take a pixel-by-pixel mean of all maps in that bin. Many pixels in a given map are masked so we also make a mean stack of the masks and divide this out to correctly normalize the mean in each pixel. No weighting is done for ease of comparison to the simulations.

A key step in this process is to correct observations for the effect of the point spread function (PSF). The PSF blurs images, resulting in dense regions appearing less dense (and vice versa of course). Our method for correcting for the effect of the PSF uses a parametric model to account for the effects of the PSF on the radial light distribution. To do this, we fit the light distribution (or derived physical quantity) of each stack with a Sérsic model (Sérsic 1968) using `GALFIT` (Peng et al. 2002). We fit a single Sérsic model letting

the brightness, effective radius, Sérsic index, centroid, projected axial ratio, and position angle be free and forcing the background level to be zero. The fit is found by convolving each model with the PSF and computing reduced χ^2 . All images are background subtracted and their backgrounds have been tested and found to be zero. Forcing the background to zero allows `GALFIT` less freedom to fit the wings of the profile. With these best-fitting parameters, we create a model not convolved with the PSF and add the residuals from the fit. This means that regions of the fit in which the image deviates from the model will be accounted for. The resulting ‘PSF-corrected’ image will have the bulk of its light corrected for the PSF but the residuals will not be (e.g. Szomoru et al. 2010).

There are of course several shortcomings with this methodology. First, this method corrects based on a single, axisymmetric Sérsic profile. This is a reasonable approximation for the mass profile of a high-redshift galaxy but real galaxies are of course more complicated. This model effectively reconstructs the radial profile of the light but will not e.g. deconvolve non-axisymmetric features at larger radii, like clumps or spiral arms. While this means that individual images are not as they would be without the PSF, we average over these types of features twice: once in the stack and again in computing the radial profile, so it is not important for this analysis. Because on average the profiles of both mass and star formation peak in the centres of galaxies (see e.g. Nelson et al. 2016), the thing that is most important for us is to replace the light into the centre so it is less important for e.g. spiral arms or clumps at large radii to be deconvolved from the PSF. Secondly, because we stack galaxies with different radii, the stack will have a steeper profile than any of the galaxies do intrinsically. The resulting fit will typically have larger Sérsic index than the average of individual galaxy images and plausibly put too much light back in the centre. We acknowledge that this step may induce a feeling of unease in the uninitiated but it is necessary and the best we can do with current tools. Ideally, our SED modelling would account for the effects of the PSF so this step would not be required, however, a tool of this kind does not yet exist.

Radial profiles are computed in circular apertures. To generate specific star formation rate profiles from the equivalent width profiles, we scale the integral of the $H\alpha$ profile to the mean total star formation rate from `Prospector` described above and the JH_{F140} to the stellar mass. We also normalize the SED modelled profiles of stellar mass and star formation to the mean integrated values from `Prospector`. Error bars are computed by bootstrap resampling the stacks. The sSFR profiles are the SFR profiles divided by the M_* profiles.

To summarize (and make the order of operations clear): we make maps of $H\alpha$, $F140W$, stellar mass, and dust attenuation for all galaxies where they are available and then stack all available maps for a given bin. For method two, the stacked dust attenuation map is applied to the stacked $H\alpha$ map. Next, all stacks are PSF-corrected, the radial profiles are computed for each $H\alpha$, JH_{F140} , stellar mass, and $H\alpha$ corrected for dust, and finally quotients are performed for each pair.

Two observational issues merit a (somewhat) brief discussion before moving on, with both most strongly affecting the sSFR profiles of massive galaxies. First, it is possible that some fraction of the central light comes from an AGN: both the broad-band emission and in particular the $H\alpha$ emission. To estimate the possible extent of this effect, we subtract observational estimates of the contribution of AGN to our observed $H\alpha$ emission from the literature. Förster Schreiber et al. (2014) and Genzel et al. (2014) find that in their sample of $z \sim 2$ galaxies with a detected broad velocity component, an average of 37 per cent of the nuclear $H\alpha$ flux comes from this broad component that they attribute to AGN-driven winds (rather

than star formation). Additionally, because of the low resolution of the G141 grism, the $H\alpha$ line we observe is contaminated by $N\text{II}$. In these same studies, the authors find nuclear $N\text{II}/H\alpha = 0.55$ in stacks of galaxies with a broad line detection. That being said, in the galaxy population writ large, Förster Schreiber et al. (2019) find fairly flat $N\text{II}/H\alpha$ gradients. Genzel et al. (2014) find 35 per cent of galaxies with $10.5 < \log(M_*/M_\odot) < 11$ have a broad component. Accounting for these effects reduces the observed central sSFR by 25 per cent. We use this as the default in our analysis but note it has a minimal effect.

Secondly, age gradients will affect the observed sSFR profiles in high-mass galaxies. Older stellar populations emit less light per unit mass than younger stellar populations. In massive galaxies on and below the main sequence, we expect the centres to be older than their outskirts. Hence, the stellar mass profiles of these galaxies are likely steeper than we infer from the JH_{F140} light profiles. This effect can be seen in the sSFR profiles based on resolved SED fitting that become more centrally depressed at high mass on and below the main sequence (see Fig. A1). Above the main sequence, on the other hand, the mass-to-light ratio gradients may be inverted due to ongoing enhanced central star formation, resulting in stellar mass profiles that are shallower than indicated by the JH_{F140} light profiles. Additionally, extra dust attenuation toward $H\text{II}$ regions may become more important towards the high surface density star formation present in the centres of high-mass galaxies above the main sequence. As can be seen in Fig. A1, the sSFR profile based on SED modelling has a higher central sSFR than that based on $EW(H\alpha)$. Because of the importance of these effects at high masses, we take the SED modelled sSFR profiles as the default for Fig. 3.

3 SIMULATION DATA

3.1 The TNG50 simulation

TNG50 is a magnetohydrodynamical cosmological simulation of galaxy formation (Nelson et al. 2019c; Pillepich et al. 2019) incorporating the new TNG model for galaxy formation physics (Weinberger et al. 2017; Pillepich et al. 2018). It is the highest resolution member of the IllustrisTNG family (TNG from now on), The Next Generation of the Illustris project. This is the most computationally demanding run of the simulation suite, requiring 130 million CPU hours (see Pillepich et al. 2019; Nelson et al. 2019b, for more details). TNG50 evolves a total of 2×2160^3 total initial resolution elements – half dark matter particles, half gas cells – with the AREPO code which uses an adaptive moving mesh (Springel 2010).

TNG50 evolves dark matter, gas, stars, black holes, and magnetic fields from $z = 127$ to $z = 0$ within a cubic volume of 51.7 Mpc side length. It has a density-dependent resolution in gaseous star-forming regions of 70–140 pc (see discussion of the numerical resolution in TNG50 discs in Pillepich et al. 2019). The *average* size of star-forming gas cells, i.e. gas with density $> 0.1\text{cm}^{-3}$, is ~ 100 physical parsecs; at higher density the resolution is even better, while at lower density the resolution is worse (see discussion of resolution on different scales in TNG50 in Nelson et al. 2019b). TNG50 provides a numerical resolution more typical of zoom simulations of single galaxies, but for ~ 1600 galaxies with $10^9 < M_* < 10^{10} M_\odot$ and ~ 530 with $10^{10} < M_* < 10^{11} M_\odot$ at $z \sim 1$.

The baryon mass resolution is $8.5 \times 10^4 M_\odot$, meaning that stellar particles as well as gas cells have roughly this mass on average. The gravitational softening length of the dark matter and stars is 0.3 kpc, whereas the softening for gas is fully adaptive down to a minimum of 74 pc. These are Plummer equivalent values, which is the spatial scale

beyond which deviation from Newtonian gravity is negligible (see discussion in Springel et al. 2020, for further technical details). The model is intentionally designed to avoid resolving the cold phase of the interstellar medium, meaning that individual star-forming clouds are treated with a sub-grid model (Springel & Hernquist 2003). TNG50 enables us to resolve much thinner discs (i.e. smaller scale heights), in both the stellar and $H\alpha$ -traced star-forming gas components, with scale heights down to $h \sim 200$ pc. These values are converging, but not yet fully converged, at TNG50 resolution (we refer to the detailed discussion in Pillepich et al. 2019).

The TNG model was designed to overcome several shortcomings identified in the original Illustris simulation (henceforth referred to simply as Illustris; Genel et al. 2014; Vogelsberger et al. 2014b; Sijacki et al. 2015). For instance, the effective radii (of the stellar mass) in Illustris were larger than observed (Genel et al. 2018; Pillepich et al. 2018), the distribution of galaxy colours showed only a weak bimodality between red and blue (Vogelsberger et al. 2014a; Nelson et al. 2018), and the gas fractions of groups and clusters was too low (Genel et al. 2014) in comparison to observational estimates. In TNG, the models for feedback from star formation and AGN were subsequently modified, as described below. Furthermore, the parameters of the TNG model were chosen to provide a better match to a few key observations including the cosmic star formation history and the following at $z = 0$: the galaxy stellar mass function, stellar mass–halo mass relation, supermassive black hole–galaxy mass relation, size–stellar mass relation, and gas fraction within group-mass haloes.

The TNG physical model for galaxy formation includes several physical process thought to be important to galaxy evolution that are implemented at the spatial and mass resolution of the simulation. In addition to gravity and hydrodynamics, the model includes gas cooling and heating, star formation, aging of single age star particles, chemical enrichment of the interstellar medium, and feedback from supernovae and super massive black holes (SMBHs).

Star formation is modelled with the simple density threshold-based parametrization of Springel & Hernquist (2003). In such a prescription, gas is stochastically converted into star particles once its density exceeds $n_H = 0.1\text{cm}^{-3}$ on a time-scale determined such that the galaxy-wide empirical Kennicutt–Schmidt relation (Kennicutt 1989) is broadly reproduced.

As in any model of galaxy formation, feedback from stars and black holes is essential. Supernova feedback associated with star formation drives galactic scale outflows. In TNG, these outflows are launched directly from star-forming gas with energy proportional to the local and instantaneous star formation rate. There are several changes to the Illustris star formation-driven wind model in TNG: the wind injection is isotropic rather than bipolar; the velocity of wind particles now scales with redshift and has a floor; and the energy now depends on metallicity and has a thermal component (Pillepich et al. 2018). The net result is that the star formation driven winds in TNG are faster at all masses and times and generally more effective at preventing star formation.

The TNG50 model for feedback from SMBHs is described in detail in Weinberger et al. (2017): SMBH feedback comes in two flavours, decided by the rate at which the black hole is accreting nearby gas. In the high accretion rate flavour, thermal energy is injected continuously into the surrounding gas, as in Illustris (Di Matteo, Springel & Hernquist 2005; Springel, Di Matteo & Hernquist 2005). At low accretion rates, kinetic energy is injected into the surrounding gas as a time-pulsed, oriented wind in a different random direction at each SMBH time-step. By contrast, in Illustris, highly bursty thermal energy was injected into large (~ 50 – 100 kpc) bubbles

displaced away from the central galaxy (Sijacki et al. 2007). The new AGN feedback model, particularly the kinetic mode, effectively quenches galaxies that reside in intermediate to high-mass haloes, including realistic gas fractions (Weinberger et al. 2017; Pillepich et al. 2018).

3.2 SFRs from TNG50 and other galaxy properties

In this work, for all galaxies we take the galaxy stellar mass to be the total mass of all star particles that are gravitationally bound to each subhalo, according to the SUBFIND halo finder (Springel et al. 2001). We take the star formation rate to be the sum of the individual star formation rates of all individual gas cells in each subhalo. These are thus instantaneous star formation rates and total masses. While this is what we attempt to measure in observations, as explored in depth in Donnari et al. (2019, 2021), aperture corrections and imperfect star formation tracers make this inexact, complicating comparisons between observations and simulations. However, we attempt to make our comparison as consistent as possible.

As with the 3D-HST data, we also exclude from the simulated galaxy analysis those with very low SFRs: $t_{\text{double}} < 20t_{\text{Hubble}}(z)$. This cut in the simulated sample automatically removes completely quenched objects or galaxies whose SFRs are so low that they fall below the resolution limit of TNG50; i.e. objects whose $\text{SFR} \equiv 0$.

Furthermore, when comparing the distribution of SFRs about the main sequence in observations and simulations (Section 4.2) it is essential to account for observational uncertainties. To do this, in observations instead of looking at simply the best-fitting value of the SFR, we use the full information about the probability density function (PDF) of the fit. To measure the scatter of the main sequence we sum the probability density function of each galaxy’s SFR instead of just looking at the distribution of the best-fitting values. We apply the same treatment to the SFRs from the simulation. We assign an observed PDF to each SFR and sum the PDFs to determine the scatter of the main sequence in TNG50. In this way, we account for observational uncertainties in the comparison between observations and simulations.

3.3 Radial profiles of sSFR in TNG50

The standard approach to making radial profile from simulations is to rotate galaxies to face on then extract profiles in circular annuli. This is of course not possible in observations, where the light from galaxies as they are oriented on the sky is what falls on our detectors. The blurring due to the point spread function (PSF) occurs on the randomly oriented image in the plane of the detector. For high S/N images, it is possible to do a PSF correction on an individual galaxy image and then deproject it before stacking. With our shallow $\text{H}\alpha$ images, however, a PSF correction is not possible on individual galaxy images, it is only possible on a stack. We therefore cannot deproject the observed $\text{H}\alpha$ images and instead project the TNG50 particle distributions to mimic the observations.

Maps of stellar mass and star-forming gas cells are made by projecting particles and cells on to a grid of 121^2 pixels representing a physical size of 60^2 kpc, or $0.5 \text{ kpc pixel}^{-1}$ using the methods developed in Diemer et al. (2019) and Tacchella et al. (2019). Each particle/cell is distributed on to pixels according to the kernel smoothing used by the simulation. This includes all particles/cells bound to the galaxy according to the SUBFIND halo finder. The centroid is defined as the co-moving centre of mass of the subhalo calculated by summing the mass weighted relative coordinates of particles of all types in the subhalo. We project galaxies in the

xy -plane in the simulation box to mimic the random projection of galaxies in observations. These maps are then mean stacked and we compute profiles in radial bins. As for the observations, error bars are determined by bootstrap resampling the stacks. We include the three full snapshots in the redshift range of the observations ($z = 0.7, 1.0, 1.5$).

In Fig. A2, we show the difference between the sSFR profiles derived from the standard face-on projection, the edge-on projection, and the random xy, xz, yz projections. The differences are fairly small but we include this correction for completeness. In particular, this correction has the largest effect in the highest mass bin below the main sequence, which, as we will soon see is a particularly important regime to treat accurately for this comparison.

4 THE INTEGRATED STAR-FORMING MAIN SEQUENCE: TNG50 VERSUS 3D-HST

Here, we investigate similarities and differences in the distribution of galaxies in the star formation rate – stellar mass plane at $0.7 < z < 1.5$ between observations from the 3D-HST survey (see Section 2.1) versus TNG50 cosmological hydrodynamical simulations (see Section 3). To make this comparison as informative as possible, we analyse the simulations and observations in the same way.

4.1 Locus of the star-forming main sequence

We compute running median star formation rates as a function of stellar mass for both samples. To define the main sequence, we fit these running medians with a quadratic

$$\log(\text{SFR}) = a + b \log(M_*) + c \log(M_*)^2.$$

As described in Sections 3 and 2, in both observed and simulated sample galaxies with very low SFRs are removed from the analysis.

Fig. 1 shows the distribution of galaxies in the $\text{SFR}-M_*$ plane from 3D-HST (dark orange points) and TNG50 (blue points) as well as the SFMS fits to the median SFRs (dark orange versus light orange curves). The median fits are remarkably similar between TNG50 and 3D-HST: they are within 0.1 dex at all masses $9 < \log(M_*/M_\odot) < 11$. The SFMS are so similar in fact that one might be tempted to conclude the first author bungled the plotting and used the same array twice. We assure the reader this is not the case: these are truly nearly identical. That being said, there remains of order ~ 0.1 -dex uncertainty in this comparison due to aperture effects and the time-scale on which the SFR is measured, as described in Donnari et al. (2019).

Let us not lose sight of the main point, however: the SFMS in the TNG50 simulation and observations from 3D-HST are in remarkable agreement. This is surprising given the longstanding 0.1–1 dex offset between the SFMSs in observations and simulations at $z = 1 - 2$ (e.g. Torrey et al. 2014; Somerville & Davé 2015; Sparre et al. 2015; Davé et al. 2016; Donnari et al. 2019). So what changed? Let us first consider the simulations. Illustris and TNG50 main sequences are shown in Fig. 1: light orange versus yellow curves. There is little change going from Illustris to TNG50 at $z \sim 1$; the slope and normalization of the main sequence have remained similar.

Turning to the observations, the SFMS from the original 3D-HST catalogues (v4.1.5; Skelton et al. 2014; Whitaker et al. 2014) as well as a literature compilation (Speagle et al. 2014) are also shown. The normalization of the main sequence at $z \sim 1$ has decreased by 0.2–0.5 dex when using the PROSPECTOR Bayesian inference framework to determine stellar population parameters compared to previous determinations. The reasons for this are complex, manifold,

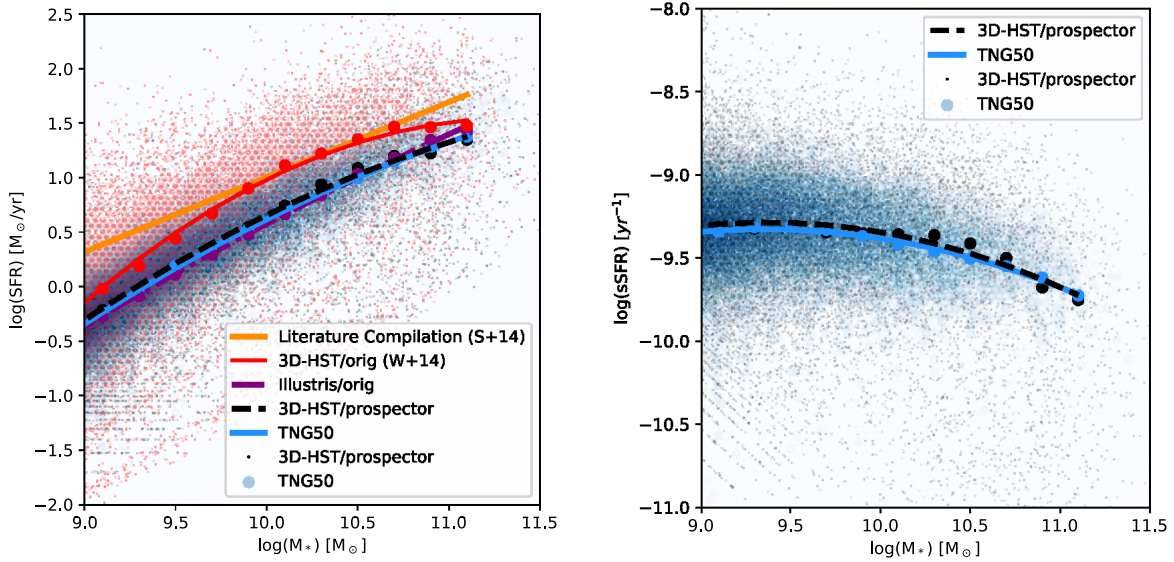


Figure 1. Left-hand panel: The star-forming main sequence (SFMS) in TNG50 (blue points) versus the 3D-HST survey black points at $0.7 < z < 1.5$. The curves show quadratic fits to the running median star formation rates. For the data, we include the original 3D-HST stellar masses and star formation rates (red points and red line: Whitaker et al. 2014; Skelton et al. 2014) and a literature compilation from Speagle et al. (2014). The new fits from *Prospector* infer stellar masses 0.1–0.3 dex higher and star formation rates 0.1–1 dex lower resulting in an SFMS with a normalization systematically lower by ~ 0.2 –0.5 dex. We also show the SFMS from the original *Illustris* simulation (purple line). Right-hand panel: same as the left-hand panel but with sSFR instead of SFR on the y-axis and stripped down to show only the comparison of TNG50 and 3D-HST/*Prospector*. The slope and normalization of the SFMS in the simulations are remarkably consistent with observations at this redshift, due to the newly inferred values from the data.

Table 1. Coefficients in the fit to the star-forming main sequence in the TNG50 simulation versus observations from the 3D-HST survey both original v4.1.5 and updated with *Prospector*. $\log(\text{SFR}) = a + b \log(M_*) + c \log(M_*)^2$.

Data/sim	a	b	c
3D-HST/ <i>Prospector</i>	−22.13	3.74	−0.146
TNG50	−20.46	3.38	−0.127
3D-HST/orig	−37.48	6.87	−0.302
<i>Illustris</i> /orig	−14.21	2.08	−0.060

and being explored in detail in Leja et al. (in preparation) but we briefly summarize our current understanding here. First, derived stellar masses increase when adopting a non-parametric instead of a parametric star formation history. Stars formed early are faint and have an extremely small impact on the observed galaxy SED – they may contribute significantly to the galaxy mass but very little to the light. These stars can be easily missed if the continuity prior is at all weighted against them as may be the case with commonly adopted tau and delay-tau models. Whereas with non-parametric star formation histories, the continuity prior is not weighted against early star formation and has been shown to lead to significantly improved stellar masses in SED fitting (Leja et al. 2017, 2019; Lower et al. 2020; Johnson et al. 2021). In addition to the new stellar masses being higher, the star formation rates are lower. At the high-mass end this largely owes to *Prospector* accounting for infrared emission due to dust heated by older stellar populations and supermassive black holes rather than star formation (see Leja et al. 2019, for more information). Thus, the long-standing 0.1–1 dex offset between the SFMS in observations and simulations at $z \sim 1$ disappears in this work not due to changes in the simulations but rather to changes in the stellar population parameters inferred from observations. Values for the coefficients in the $z \sim 1$ main-sequence fit (equation above) are listed in Table 1.

Table 2. Scatter in the SFMS in 3D-HST/*Prospector* versus TNG50. This is measured in bins of stellar mass with a width 0.5 dex including observational uncertainties on both the observations and simulations. The ‘scatter’ here refers to the width of the region that contains 68% of the distribution (see Section 4.2 for more details.).

Mass bins	3D-HST/ <i>Prospector</i>	TNG50	Ratio
$9 < \log(M_*) < 9.5$	0.41	0.33	0.81
$9.5 < \log(M_*) < 10$	0.38	0.33	0.88
$10 < \log(M_*) < 10.5$	0.45	0.32	0.72
$10.5 < \log(M_*) < 11$	0.57	0.33	0.58

As shown in Torrey et al. (2014), the SFMS in simulations is fairly insensitive to the nature of the feedback prescription. This is also the case in a gas-regulator model based on mass conservation where in quasi-steady-state the sSFR follows the cosmological specific accretion rate (e.g. Dekel & Mandelker 2014) with the latter estimated from theory (e.g. Dekel et al. 2013). The integrated main sequence is thus not a particularly discerning validation of a simulation’s feedback model. As we will show in the next section, this is not the case when looking at the resolved properties of star formation across the main sequence.

Furthermore, Leja et al. (2015) showed that earlier measurements of the SFMS and the evolution of the stellar mass function were not self-consistent in observations: the SFMS dramatically overpredicted galaxy stellar mass growth. In the simulations, the SFMS and stellar mass growth are obviously self-consistent and hence it is unsurprising that simulations could not simultaneously match both the observed, non-self-consistent main sequence and mass function. With data that are self-consistent, the simulations can match both as they are directly coupled.

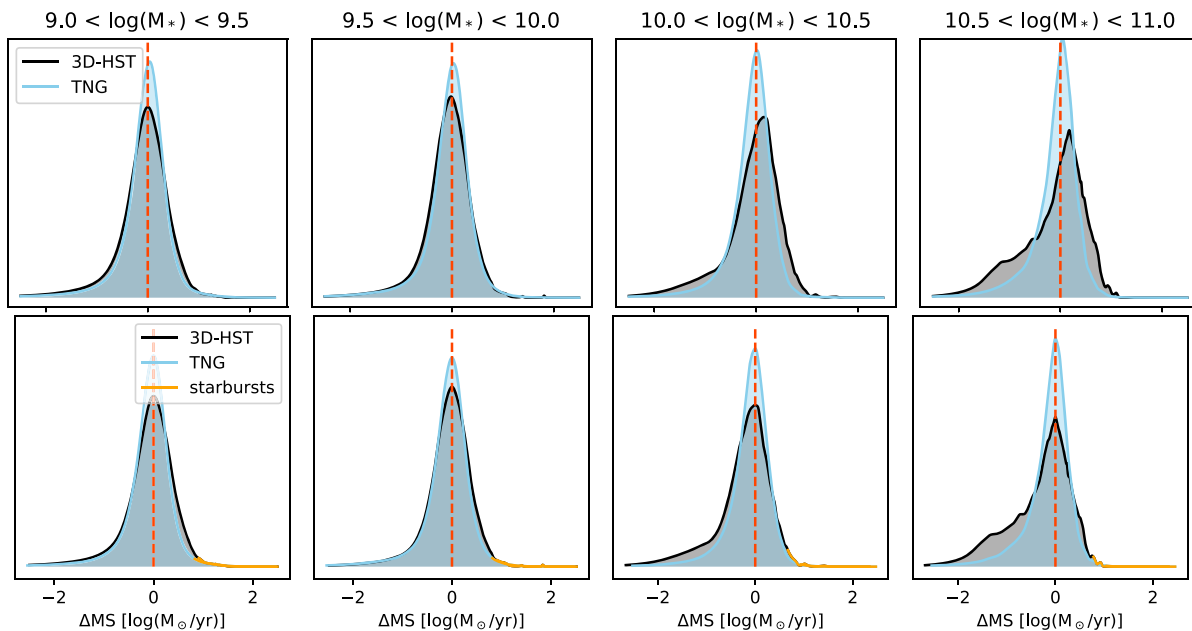


Figure 2. Top: Distribution of simulated and observed galaxies around the main sequence in bins of stellar mass. We contrast the 3D-HST data (black), TNG50 simulation (light blue). Although the width of these distributions is broadly consistent between the simulations and observations at lower galaxy stellar mass, the simulated scatter is smaller than observed at high ($M_* > 10^{10} M_\odot$). Furthermore, at high masses the distribution is more skewed to low SFRs in observations than in TNG50. Bottom: As above, except with the distribution shifted to the ridgeline of the distribution of star formation rate rather than the median. With this shift applied, the shape of the distribution of galaxies above the main sequence is similar between observations from 3D-HST/prospector and TNG50. The orange solid line shows the definition of ‘starbursts’ used in Section 4 following Rodighiero et al. (2011) and Sparre et al. (2015): $>2.5\sigma$ above the main sequence.

4.2 Width and outliers of the star-forming main sequence

Although the medians are nearly identical between TNG50 and *Prospector*/3D-HST, the distribution of galaxies about these medians is not, even when accounting for observational uncertainties in our treatment of the simulations. We look at the distribution of the distance of galaxies from the median fit (ΔMS) in bins of stellar mass (see Fig. 2). Investigating the shape of this distribution requires properly accounting for observational uncertainties. *Prospector* returns a probability density function (PDF) for each parameter it fits. In each bin, we sum the PDFs of SFR normalized to the main-sequence fit then normalize the overall distribution to have an area of 1. To make the distribution from simulations more directly comparable, as mentioned in Section 3.2, we assign an observed PDF to each SFR in the simulation by drawing randomly from the observed galaxies with similar masses and SFRs (as the width of the PDF is dependent on these quantities). We then sum the TNG50 PDFs in the same way as the observed ones. In other words, we add observational uncertainties to the simulated SFRs so that the scatter is directly comparable.

Fig. 2 (top row) shows this comparison – the distribution of simulated and observed galaxies around the main sequence in bins of stellar mass. We remind the reader that observed and simulated galaxies with very low SFRs ($t_{\text{double}} < 20t_{\text{Hubble}}(z)$) are not considered in this analysis. At all masses, the TNG main sequence is narrower than the observations. That is, there is less scatter in the SFRs of the simulated galaxies than there is amongst the observed galaxies. We note that we use the instantaneous SFR in the simulations and the SFR averaged over 30 Myr in observations. The scatter of the main sequence measured from instantaneous SFRs will be larger than those averaged over longer time-scales (e.g. Caplar & Tacchella 2019; Donnari et al. 2019; Tacchella et al. 2020) so likely

the difference in the scatter is even larger than we see here. This is less dramatic below $\log(M_*) = 10$ and more dramatic above. We quantify this difference in width by computing the width of the region that contains 68 per cent of the distribution. These values are listed in Table 2. For $9 < \log(M_*) < 10$, we find the simulations are 80–90 per cent the width of observations. For $10 < \log(M_*) < 10.5$, the difference grows to 70 per cent; for $10.5 < \log(M_*) < 11$ –60 per cent.

We speculate that one cause of the narrower scatter in TNG than observations could be the TNG model assumption of fixed parameter values to describe feedback, e.g. as a function of galaxy mass or other properties. In the case of AGN feedback, the amount of energy from accretion that couples to the gas around black holes is such a value. Such an assumption may be an oversimplification, and could also be related to the finding that the scatter in physical relations, such as that between black hole mass and galaxy properties, may also be relatively small (e.g. Terrazas et al. 2020). Similar arguments may be true of the prescriptions for star formation driven winds which may impact the scatter at the low-mass end. Allowing for some distribution in the feedback efficiency may make the scatter in the simulation more closely match observations but is somewhat arbitrary. Alternatively, holding the physical model fixed, higher numerical resolution would enable the simulations to resolve shorter temporal events such as starbursts (Sparre & Springel 2016), increasing the scatter in simulated SFRs further.

The distribution is more skewed towards low SFRs in observations. While in TNG50, the distributions are self-similar at all masses, in observations they become more skewed towards high masses. We quantify this by measuring the skewness of the distributions of the simulated versus observed galaxies based on the ridgeline of the distribution instead of the mean as in the standard definition. For this

work, we define the skewness as

$$\mu_3 = \frac{\sum_i^N (\log(\text{SFR}) - \log(\text{SFR}_{\text{ridge}}))^3}{(N-1) * \sigma^3},$$

where $\log(\text{SFR}_{\text{ridge}})$ is the ridgeline of galaxies in the SFR– M_* plane and σ is the standard deviation of galaxies about this ridgeline. At $10.5 < \log(M_*/M_\odot) < 11$, the observed distribution of SFR has a skewness of -1.8 while TNG50 has -0.4 . We note that, from the observational side that SFRs of low-sSFR galaxies are the most dependent on how the photometry is modelled, in particular how the star formation history is parametrized. On the simulation side, the relative lack of low-SFR galaxies in TNG50 may be related to the AGN feedback model. In TNG, kinetic mode AGN feedback efficiently shuts down star formation, while the thermal quasar-mode is comparably inefficient (Weinberger et al. 2018). Within the model, every black hole is in one of these two modes, with low-mass, rapidly accreting black holes (living in low-mass or high-redshift galaxies) being in the thermal mode. Once the accretion rate (relative to the Eddington accretion limit) drops sufficiently low, the feedback switches to a kinetic mode, leading to a rapid decline in sSFR as a function of black hole mass, as well as stellar mass and other properties of the simulated $z \sim 0$ galaxy population (Habouzit et al. 2019, 2020; Li et al. 2020; Terrazas et al. 2020). We speculate that, similarly, $z \sim 1$ galaxies in TNG50 quickly quench whereas in the real Universe massive galaxies seem more likely to tarry below the main sequence before becoming fully quenched – such quenching time-scales can be compared in future work.

Furthermore, at $M_* > 10^{10} M_\odot$ above the main sequence an insufficient number of starbursts as compared to the real Universe was noted in the original Illustris (Sparre et al. 2015). We similarly quantify this by comparing the fraction of star formation that occurs more than 2.5σ above the main sequence in 3D-HST and TNG50 (as in Rodighiero et al. 2011; Sparre et al. 2015). We calculate this fraction based on both ridgelines of the distributions. Our definition is shown in Fig. 2 (bottom row). At high masses, TNG50 has a ridgeline which is ~ 0.15 dex lower than observations despite the medians being the same. We also use the scatter as a function of mass from TNG50 to compute this for both observations and TNG50 because the scatter is significantly smaller in TNG50 than observations at high masses.

For mass bins [9,9.5], [9.5,10], [10,10.5], [10.5,11] in observations we find the following fractions of star formation occurring in starbursts [12, 10, 6, 2 per cent] and for TNG50 we find [15, 13, 5, 3 per cent]. After accounting for the difference between the ridgeline and median of the distribution of SFRs, using the same value for scatter, and accounting for errors on the observed SFRs, the fraction of star formation occurring in ‘starbursts’ is very similar in observations from 3DHST/Prospector and TNG50. This represents a key success of the simulation, likely due to its higher resolution, and demonstrates that there is no intrinsic inability of the TNG galaxy formation model to produce vigorous starburst events. The residual tension with the TNG50 SFRs is rather the shape of the distribution from the ridgeline to low SFRs.

5 SSFR PROFILES IN TNG50 VERSUS 3D-HST

Here, we compare the average radial profiles of sSFR in galaxies on, above, and below the SFMS in observations from the 3D-HST survey at $z \sim 1$ and the TNG50 simulation. The derivation of the profiles is described in Section 2.4 for the observations and Section 3 for the simulations.

The sSFR profiles are a powerful diagnostic to understand where the galaxies are growing. A flat sSFR profile indicates that the stellar mass doubles at all radii with the same pace, implying a self-similar growth of the stellar mass density profile. An increasing sSFR towards the outskirts implies that the galaxy grows stellar mass faster in the outskirts than in the centre (stellar mass content of the galaxy grows in size), while a decreasing sSFR towards the outskirts is consistent with a galaxy that decreases its size.

5.1 Inside-out quenching

A key result of this paper is that star formation is quenched from the inside-out, which in the simulations is caused directly by AGN feedback. Fig. 3 shows that below the SFMS at $10.5 < \log(M_*) < 11$, the sSFR profiles are strongly centrally suppressed in both TNG50 and in observations (e.g. Nelson et al. 2016; Belfiore et al. 2018; Ellison et al. 2018; Tacchella et al. 2018; Morselli et al. 2019), which we interpret as inside-out quenching. In TNG50, this centrally suppressed star formation is a direct signature of locally acting AGN feedback (see Nelson et al. 2019b).

In TNG50 both kinetic and thermal feedback act on the gas immediately surrounding the black hole. The TNG black hole feedback model introduces powerful ‘kinetic’ kicks when a black hole reaches a certain mass (Weinberger et al. 2017; Nelson et al. 2019b). These kicks evacuate gas from the very centre of the galaxy (Zinger et al. 2020), and can provide enough feedback energy to gravitationally unbind some amount of gas from the galaxy. It has recently been shown that this feedback mode also produces outflows around TNG50 Milky Way and M31-like galaxies similar to the observed Fermi and eROSITA bubbles (Pillepich et al. 2021). As described in Terrazas et al. (2020), galaxies in this state are in the process of unbinding their gas starting from the very central regions, expanding outwards to larger radii. Observations of sSFR profiles across the main sequence clearly constrain the implementation of AGN feedback in these models.

At this juncture, one thought the reader may be having is ‘yes, but is the inside-out quenching *really* due to AGN feedback or could it be caused by something else?’ To address this question, we perform the same analysis described above on a ‘TNG variation’ simulation box (see Pillepich et al. 2018) that was run without kinetic wind AGN feedback. All other aspects of the model remain unchanged. The results of this experiment, in Fig. 4, show that without AGN kinetic winds, star formation is not centrally suppressed. We therefore conclude that in TNG50, inside-out quenching is caused by AGN feedback, specifically kinetic winds. One caveat here is that the run without kinetic winds produces a relatively unrealistic galaxy population, with properties not calibrated nor tested against observations. That said, this test shows that in the TNG simulations, inside-out quenching does not appear to be caused by gravitational quenching or star formation driven feedback, it is caused by feedback from AGN. We note, however, that this is not a unique solution to explaining inside-out quenching in the real Universe: in other simulations centrally suppressed specific star formation rates have other causes like gas depletion due to high central star formation rates (e.g. Tacchella et al. 2016b) or massive bulges (e.g. Martig et al. 2009; Dekel et al. 2020). We also note that other simulations find centrally enhanced sSFRs (rather than the suppressed sSFRs found in the real universe): Orr et al. (2017) below the main sequence in FIRE, and Starkenburg et al. (2019) in the green valley in Illustris and EAGLE.

This inside-out quenching signature is not seen in the original Illustris simulation, where low-state AGN feedback acts non-locally. In Illustris, bubbles are blown at galactocentric distances of 50–

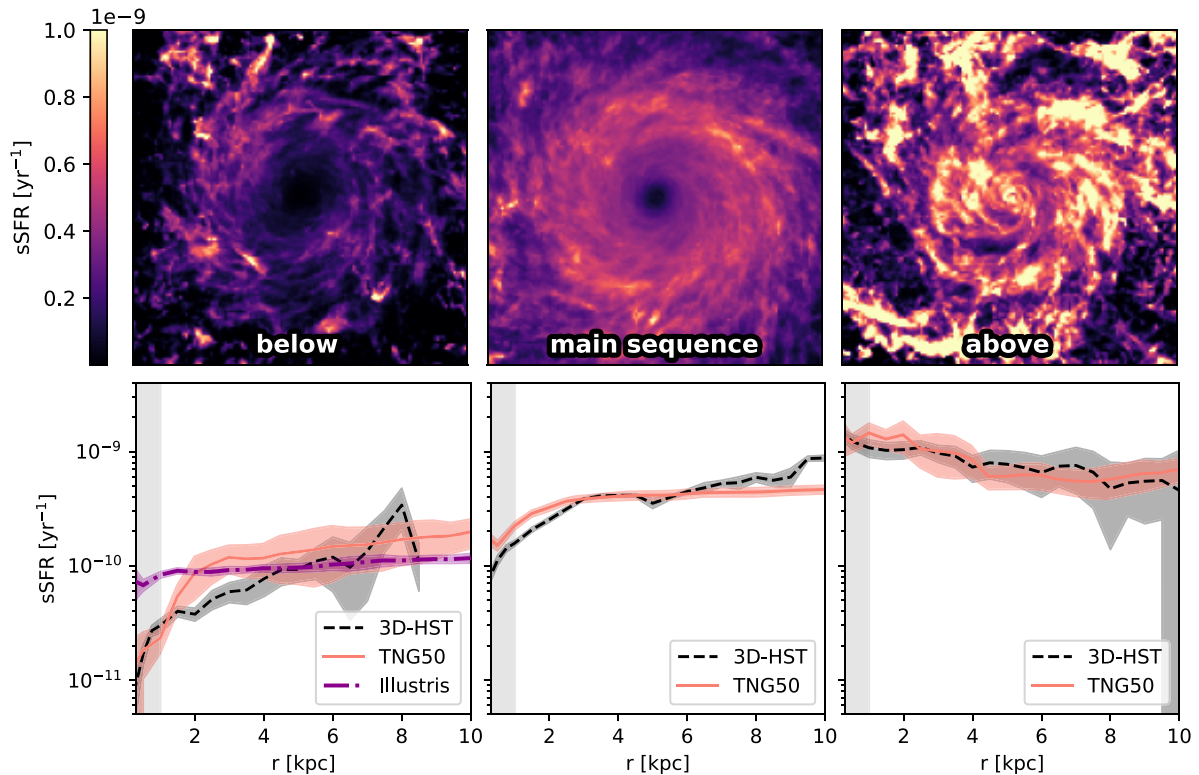


Figure 3. Top row: stacks of sSFR in TNG50 face-on. Bottom: sSFR radial profiles of massive galaxies, with $10^{10.5} < M_*/M_\odot < 10^{11}$ at $z \sim 1$. We contrast profiles inferred from observations with 3D-HST (dashed black curves) against the outcome of the TNG50 hydrodynamical simulation (solid curves), as a function of offset from the SFMS: galaxies which reside below (left), on (centre), and above (right). Note the profiles are constructed from stacks at random orientations, not the face-on ones shown. The shaded regions around these lines represent the 1σ uncertainty from bootstrap resampling the stacks. In all cases, the TNG50 simulation broadly reproduces both the normalization and shape of the observed sSFR radial profiles. A key result of this work is that quenching galaxies (left) exhibit a clear central SFR suppression in the data as well as in TNG50. This supports the scenario of inside-out quenching, which in TNG50 arises due to a central, short time-scale, ejective supermassive black hole feedback mechanism at low accretion rates. This is not the case with the jet-inflated bubble black hole feedback model in Illustris as shown by the dash-dot purple line. The vertical grey shaded region is inside the observed PSF.

100 kpc and consequently have a hard time propagating back into the denser gas to affect the centre of the galaxy. Hence, the sSFR profiles in Illustris are not centrally suppressed. The immediate question here is if this difference is due to the different physics in Illustris and TNG50 or the different resolution. In Fig. 5, we also disentangle the impact of resolution, comparing TNG50-1 to TNG50-2, the analogous simulation run with eight times worse mass resolution (two times worse spatial resolution). As shown through the comparison to the lower resolution version of TNG50, this is not a resolution effect but due to the physics in the simulation. Notably, the original Illustris simulation, with its rather different physical mechanism for AGN feedback at low accretion rates, based on jet-inflated bubbles heating the ICM at distances of tens of kpc or more from the galaxy, does not reproduce the central SFR profile suppression seen in data. This different manifestation between the two feedback models is clearly constrained by the observations.

In general, the TNG AGN feedback model produces sSFR profiles which are in better agreement with observations than the original Illustris simulation. In quantitative detail there remain small differences between the observed and TNG50 sSFR profiles at high masses (i.e. $\log M_* > 10.5$) below the main sequence. While the sSFR profiles agree at the centres, for $2 < r < 4$ kpc TNG50 is about a factor of 2 higher than observations. This implies that the central suppression of SFR does not extend to sufficiently large radii as seen in the data. This could be related to the modelling

of the interstellar medium in this simulation: in particular, there is no explicit multiphase medium with cold clouds embedded in a hot, volume filling component, but cells have a single, volume averaged density value and a pressure according to an effective equation of state (Springel & Hernquist 2003). This means that AGN-driven winds that interact with this medium impact the entire mass budget, while a situation where the wind propagates in low-density channels while cold clouds continue forming stars (e.g. Dugan, Gaibler & Silk 2017) is hindered in the TNG simulations. It is possible that the effect of AGN winds would differ with a more realistically modelled ISM – a scenario testable with future simulations.

In summary, based on observations of centrally suppressed average sSFRs in galaxies below the main sequence, we find that massive galaxies quench from the inside-out. In the TNG simulations, the details of how supermassive black hole feedback are implemented and, in particular, how this feedback energy physically affects, heats, and redistributes gas appears to zeroth-order consistent with constraints from the observed star formation rate radial profiles on scales of a kiloparsec. While not necessarily the case in the real Universe, in TNG50, inside-out quenching is caused by AGN feedback.

5.2 Flat sSFR profiles across the star-forming main sequence

Average sSFR profiles of galaxies on, above, and below the SFMS in observations and simulations are shown in Fig. 5. The main takeaway

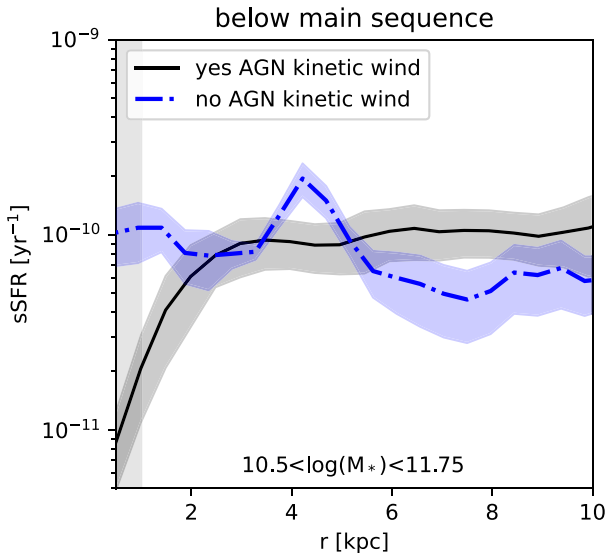


Figure 4. sSFR profiles of high-mass galaxies below the main sequence ($10^{10.5} < M_* < 10^{11.75} M_\odot$). This is the region of parameter space in which we expect the effects of AGN feedback to be most pronounced. Here, we compare two smaller volume ‘TNG variation’ simulations, each of 25 cMpc h^{-1} side-length. One uses the fiducial TNG model unchanged, while the other excludes AGN-driven kinetic winds. The difference is stark: the centrally suppressed star formation seen in the fiducial TNG50 model including AGN-driven kinetic winds disappears when this feedback channel is turned off. This suggests that in the TNG simulations, it is the kinetic mode AGN feedback that causes inside-out quenching.

is that the sSFR profiles across the main sequence in TNG50 are remarkably similar to those in observations. As shown in Fig. 6, With few exceptions, at all masses and radii the observed and simulated sSFR profiles lie within 0.3 dex (a factor of 2) of each other.

This agreement is surprising; it did not have to turn out this way. The consistency shows that the spatial distribution of dense gas and the conversion of gas into stars are roughly correct in the simulation, at least relative to the existing stellar mass. This means that the physical TNG50 model governing how galaxies grow in size and build their structures across the SFMS yield high-fidelity predictions. The distribution of cold gas is set by the spatially dependent interplay between gas inflows, outflows, and star formation. The accretion of gas on to the galaxies is driven by gravity (a model about which there is less uncertainty than the others) and suppressed by feedback. TNG50 uses the Springel & Hernquist (2003) model for star formation. In this model gas above a certain density threshold is converted to stars stochastically. While this model is a simplification of reality (e.g. Semenov, Kravtsov & Gnedin 2019), on kpc scales it produces results that are consistent with observations.

Feedback has significant effects in all parts of the baryon cycle: it affects inflow rates and geometries (e.g. Nelson et al. 2015) and it determines the distribution of cold gas and hence where the galaxy can form stars. In TNG50 outflows driven by supernova feedback are launched from star-forming gas with their energy given by the star formation rate. This result means that at $0.75 < z < 1.5$ and $9 < \log(M_*) < 10.5$, the way outflows are implemented in TNG50 produces results that are on population and azimuthal average, consistent with observations on, above, and below the SFMS. We note that the agreement of a given model with observations does not imply uniqueness of this model, as alternative models may reproduce the same observation. That said, TNG50’s parametrization

of outflows and conversion of gas into stars produces galaxies that have a radial structure of new star formation over past star formation that is consistent with the real Universe.

Above the main sequence the sSFR profiles from TNG50 and 3D-HST are fairly flat. In this regime, the match with observations improved from Illustris to TNG. In Illustris, the profiles have somewhat of a negative gradient while in TNG50 (and 3D-HST observations) they do not. This is not primarily a resolution effect as the profiles in TNG-LowRes are fairly flat like those in TNG50. Instead this is likely a physical effect owing to the implementation of supernova feedback. As shown in observations as well as in TNG50 (Förster Schreiber et al. 2019; Nelson et al. 2019b), star formation driven winds are strongest above the SFMS, at least at $z \sim 1$. The implementation of these winds changed from Illustris to TNG, affecting many observable properties of galaxies, such as their metallicity gradients (Hemler et al. 2020) and circumgalactic media (Byrohl et al. 2020). Here, we see that it also affects the shape of the sSFR profiles of galaxies above the main sequence. In TNG50 wind energy has an additional scaling with the metallicity (Pillepich et al. 2018). These changes produce flatter sSFR profiles above the main sequence, more in line with observations from the 3D-HST survey at $z \sim 1$.

What do the shapes of the sSFR profiles mean for how galaxies build structurally? Across the main sequence at all masses and star formation rates, the sSFR profiles on average are fairly flat, meaning that galaxies grow largely self-similarly on average (Nelson et al. 2019c). This is consistent with the fact that the size–mass relation for star-forming galaxies has a shallow slope (e.g. Patel et al. 2013; van Dokkum et al. 2013; van Dokkum et al. 2015; Suess et al. 2019; Mosleh et al. 2020). Star formation adds stars to galaxies with close to the same distribution as the existing stars so the structure of galaxies as a population as a function of mass changes fairly slowly. This is not necessarily true of individual galaxies and in fact the purpose of this detailed comparison between observations and simulations is in service of the ability to use these simulations to track individual galaxies through time to see what drives their evolution through the SFR– M_* plane.

6 SUMMARY

In this paper, we have compared the SFMS and sSFR profiles in the TNG50 magnetohydrodynamical cosmological simulation and observations from the 3D-HST survey. TNG50 is the highest resolution iteration of the IllustrisTNG project, resolving 2100 galaxies with $M_* > 10^9 M_\odot$ at a spatial resolution of $\sim 100 \text{ pc}$ at $z \sim 1$. The 3D-HST program is a 248 orbit near-infrared spatially resolved spectroscopic survey with the *Hubble Space Telescope* that provides maps of the sSFR in thousands of galaxies at $z \sim 1$. These are complemented by a new analysis of the integrated photometry of these galaxies with the *Prospector* Bayesian inference framework, providing improved estimates for stellar masses and SFRs. These simulated and observed data sets are well-matched to determine how well the simulation can be used to understand how galaxies move through the SFMS, what causes star formation to be enhanced and suppressed, and how galaxies evolve structurally during this process.

We find that the SFMS in TNG50 is consistent to within 0.1 dex of observations from 3D-HST for all masses $10^9 < M_* < 10^{11} M_\odot$ at $0.75 < z < 1.5$ derived from *Prospector*. This is a significantly stronger agreement than previously reported for the TNG simulations in comparison to then-available observationally inferred results (Donnari et al. 2019) and a strong validation of the model in a galaxy integrated population sense (see Fig. 1). This is also better than typically reported in cosmological hydrodynamical simulations,

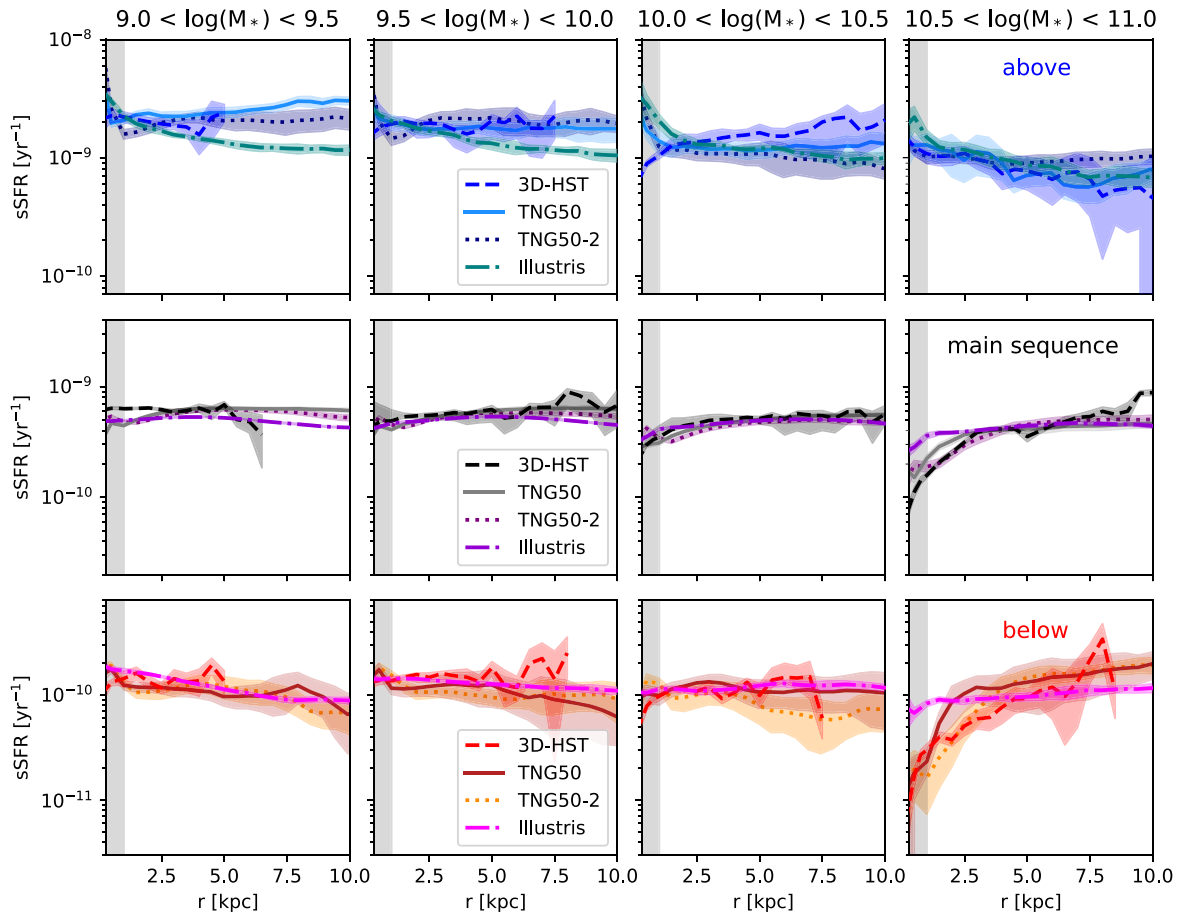


Figure 5. sSFR profiles of $z \sim 1$ galaxies across the SFMS – comparison between observations and TNG50, the original Illustris simulation, and a lower resolution version of TNG50 with resolution more similar to that of Illustris (TNG50-2). Profiles are cut off when their signal-to-noise ratio falls below 1. We find that TNG50 is more consistent with observations than the original Illustris simulation and that this is not primarily due to resolution effects. The grey shaded region is inside the observed PSF.

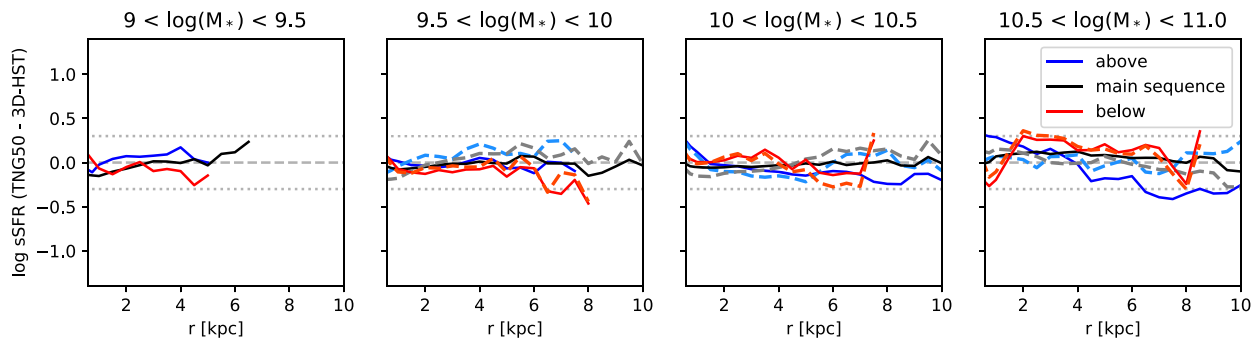


Figure 6. Difference between the sSFR profiles in 3D-HST and TNG50. As shown by the dotted grey lines, the profiles are nearly always within ± 0.3 dex (a factor of 2) of each other.

where the previous 0.2–1 dex offset between observations and simulations may be driven by the inference of stellar population parameters from observations rather than necessarily the physical model in simulations, although uncertainties remain to be tested regarding star formation histories and other aspects of the inference of stellar populations.

The newly derived stellar mass estimates are 0.1–0.3 dex higher and the star formation rates 0.1–1 dex lower than previous estimates

(see Leja et al. 2019, for more details). While the median SFRs are nearly identical between TNG50 and observations, some discrepancies do arise in the higher order moments of the SFR distribution. The scatter of SFRs around the main sequence in TNG50 is narrower at all masses than in observations, perhaps due to the fact that the model uses fixed values to describe feedback which is unrealistic. It is also self-similar while the observed SFRs skew towards lower values as mass increases (Fig. 2).

Further, we find surprisingly good agreement between the TNG50 simulated and 3D-HST observed average sSFR radial profiles of galaxies above, on, and below the SFMS. With a few exceptions, they agree qualitatively and quantitatively. They are within a factor of 2 at all masses and radii across the main sequence. Qualitatively, in both of these observations and simulations, across the main sequence, the sSFR profiles are fairly flat, meaning galaxies on average grow self-similarly regardless of where they are in the SFR– M_* plane, which is likely why the size growth of galaxies is so gradual. This means, importantly that the distribution of gas and its conversion into stars in the simulation are at least roughly correct on kpc scales.

The agreement between resolved patterns of star formation in the TNG50 simulation and 3D-HST data is particularly interesting below the main sequence at high masses, a region of parameter space that galaxies must necessarily traverse on their journey from star forming to quenched. Here, we find that both simulated and observed $z \sim 1$ galaxies exhibit depressions in sSFR in the central regions, up to a few kpc wide. The inside-out suppression of star formation in high-mass galaxies below the main sequence is similar in both 3D-HST observations and in the TNG50 simulation. This is a key signature of locally acting AGN feedback in the TNG simulations. This behaviour is not seen in the original Illustris simulation, where AGN feedback affects gas at large radii rather than acting directly from the innermost regions of galaxies. Notably, this inside-out quenching signature is also not present in a ‘TNG variation’ simulation run without AGN kinetic winds. Taken together, our results provide evidence for AGN feedback as the source of inside-out quenching in the TNG simulations.

Looking ahead, given confidence that the simulation reasonably reproduces these observations of resolved star formation activity, we can use it to interpret how galaxies simultaneously move through the SFR– M_* plane and evolve in their structural details.

ACKNOWLEDGEMENTS

The TNG50 simulation was realized with compute time granted by the Gauss Centre for Supercomputing (GCS) via the Large-Scale Project GCS-DWAR (2016; PIs Nelson/Pillepich); its lower resolution counterparts were carried out on the Draco and Hydra supercomputers at the Max Planck Computing and Data Facility (MPCDF); the original Illustris simulation was performed at the CURIE supercomputer at CEA/France as part of PRACE project RA0844 and at the SuperMUC computer at the Leibniz Computing Centre, Germany, as part of project pr85je. EJN acknowledges support of the National Hubble Fellowship Program through grant number HST-HF2-51416.001-A. ST is supported by the Smithsonian Astrophysical Observatory through the CfA Fellowship. BB acknowledges support of the Simons Foundation Flatiron Institute and is a Packard Fellow. FM acknowledges support through the Program ‘Rita Levi Montalcini’ of the Italian MUR. BAT was supported by the Harvard Future Faculty Leaders Postdoctoral Fellowship. The Cosmic Dawn Center (DAWN) is funded by the Danish National Research Foundation under grant No. 140. RKC acknowledges funding from the John Harvard Distinguished Science Fellowship. PT acknowledges support from NSF grants AST-1909933, AST-200849, and NASA ATP grant 80NSSC20K0502. We thank the reviewer, Avishai Dekel, for constructive comments which strengthened the manuscript.

DATA AVAILABILITY

The observational data underlying this article are available at archive.stsci.edu/prepds/3d-hst/. The IllustrisTNG simulations, including

TNG50, are publicly available and accessible at www.tng-project.org/data as described in Nelson et al. (2019a).

REFERENCES

- Abdurro'uf, Akiyama M., 2018, *MNRAS*, 479, 5083
- Appleby S., Davé R., Kraljic K., Anglés-Alcázar D., Narayanan D., 2020, *MNRAS*, 494, 6053
- Arnouts S., Cristiani S., Moscardini L., Matarrese S., Lucchin F., Fontana A., Giallongo E., 1999, *MNRAS*, 310, 540
- Ashby M. L. N. et al., 2013, *ApJ*, 769, 80
- Aumer M., White S. D. M., 2013, *MNRAS*, 428, 1055
- Behroozi P. S., Wechsler R. H., Conroy C., 2013, *ApJ*, 770, 57
- Belfiore F. et al., 2018, *MNRAS*, 477, 3014
- Bell E. F. et al., 2004, *ApJ*, 608, 752
- Blanton M. R. et al., 2003, *ApJ*, 594, 186
- Brammer G. B. et al., 2009, *ApJ*, 706, L173
- Brammer G. B. et al., 2012a, *ApJS*, 200, 13
- Brammer G. B. et al., 2012b, *ApJ*, 758, L17
- Brooks A. M. et al., 2011, *ApJ*, 728, 51
- Bruzual G., Charlot S., 2003, *MNRAS*, 344, 1000
- Byrohl C., Nelson D., Behrens C., Pillepich A., Hernquist L., Marinacci F., Vogelsberger M., 2020, *MNRAS*, 506, 5129
- Calzetti D., Armus L., Bohlin R. C., Kinney A. L., Koornneef J., Storchi-Bergmann T., 2000, *ApJ*, 533, 682
- Caplar N., Tacchella S., 2019, *MNRAS*, 487, 3845
- Ceverino D., Klypin A., Klimek E. S., Trujillo-Gomez S., Churchill C. W., Primack J., Dekel A., 2014, *MNRAS*, 442, 1545
- Chabrier G., 2003, *PASP*, 115, 763
- Christensen C. R., Brooks A. M., Fisher D. B., Governato F., McCleary J., Quinn T. R., Shen S., Wadsley J., 2014, *MNRAS*, 440, L51
- Cibinel A. et al., 2015, *ApJ*, 805, 181
- Conroy C., Wechsler R. H., 2009, *ApJ*, 696, 620
- Crain R. A. et al., 2015, *MNRAS*, 450, 1937
- Daddi E. et al., 2007, *ApJ*, 670, 156
- Davé R., Anglés-Alcázar D., Narayanan D., Li Q., Rafieferantsoa M. H., Appleby S., 2019, *MNRAS*, 486, 2827
- Davé R., Thompson R., Hopkins P. F., 2016, *MNRAS*, 462, 3265
- Dekel A. et al., 2020, *MNRAS*, 496, 5372
- Dekel A., Mandelker N., 2014, *MNRAS*, 444, 2071
- Dekel A., Zolotov A., Tweed D., Cacciato M., Ceverino D., Primack J. R., 2013, *MNRAS*, 435, 999
- Di Matteo T., Springel V., Hernquist L., 2005, *Nature*, 433, 604
- Diemer B. et al., 2019, *MNRAS*, 487, 1529
- Donnari M. et al., 2019, *MNRAS*, 485, 4817
- Donnari M. et al., 2021, *MNRAS*, 500, 4004
- Dubois Y., Peirani S., Pichon C., Devriendt J., Gavazzi R., Welker C., Volonteri M., 2016, *MNRAS*, 463, 3948
- Dugan Z., Gaibler V., Silk J., 2017, *ApJ*, 844, 37
- Ellison S. L., Sánchez S. F., Ibarra-Medel H., Antonio B., Mendel J. T., Barrera-Ballesteros J., 2018, *MNRAS*, 474, 2039
- Faber S. M. et al., 2007, *ApJ*, 665, 265
- Förster Schreiber N. M. et al., 2006, *ApJ*, 645, 1062
- Förster Schreiber N. M. et al., 2009, *ApJ*, 706, 1364
- Förster Schreiber N. M. et al., 2011b, *ApJ*, 739, 45
- Förster Schreiber N. M. et al., 2014, *ApJ*, 787, 38
- Förster Schreiber N. M. et al., 2019, *ApJ*, 875, 21
- Förster Schreiber N. M., Shapley A. E., Erb D. K., Genzel R., Steidel C. C., Bouché N., Cresci G., Davies R., 2011a, *ApJ*, 731, 65
- Genel S. et al., 2014, *MNRAS*, 445, 175
- Genel S. et al., 2018, *MNRAS*, 474, 3976
- Genzel R. et al., 2014, *ApJ*, 796, 7
- Giavalisco M. et al., 2004, *ApJ*, 600, L93
- Governato F. et al., 2010, *Nature*, 463, 203
- Graves G. J., Faber S. M., Schiavon R. P., 2009, *ApJ*, 693, 486
- Grogin N. A. et al., 2011, *ApJS*, 197, 35
- Guedes J., Callegari S., Madau P., Mayer L., 2011, *ApJ*, 742, 76

- Habouzit M. et al., 2019, *MNRAS*, 484, 4413
 Habouzit M. et al., 2020, *MNRAS*, 503, 1940
 Hemler Z. S. et al., 2020, *MNRAS*, 506, 3024
 Hernquist L., 1989, *Nature*, 340, 687
 Hopkins P. F., Kereš D., Oñorbe J., Faucher-Giguère C.-A., Quataert E., Murray N., Bullock J. S., 2014, *MNRAS*, 445, 581
 Ilbert O. et al., 2006, *A&A*, 457, 841
 Johnson B. D., Leja J., Conroy C., Speagle J. S., 2020, *ApJS*, 254, 22
 Johnson B. D., Leja J., Conroy C., Speagle J. S., 2021, *ApJ*, 254, 22
 Johnson B., Leja J., 2017, Bd-J/Prospector: Initial Release. [Accessed 18 Aug 2021]
 Karim A. et al., 2011, *ApJ*, 730, 61
 Kauffmann G. et al., 2003, *MNRAS*, 341, 54
 Kennicutt R. C., Jr., 1989, *ApJ*, 344, 685
 Khandai N., Di Matteo T., Croft R., Wilkins S., Feng Y., Tucker E., DeGraf C., Liu M.-S., 2015, *MNRAS*, 450, 1349
 Koekemoer A. M. et al., 2011, *ApJS*, 197, 36
 Lee B. et al., 2018, *ApJ*, 853, 131
 Leja J. et al., 2013, *ApJ*, 778, L24
 Leja J. et al., 2019, *ApJ*, 877, 140
 Leja J., Johnson B. D., Conroy C., Dokkum P. G. v., Byler N., 2017, *ApJ*, 837, 170
 Leja J., van Dokkum P. G., Franx M., Whitaker K. E., 2015, *ApJ*, 798, 115
 Li Y. et al., 2020, *ApJ*, 895, 102
 Licquia T. C., Newman J. A., 2015, *ApJ*, 806, 96
 Lower S., Narayanan D., Leja J., Johnson B. D., Conroy C., Davé R., 2020, *ApJ*, 904, 33
 Lundgren B. F. et al., 2012, *ApJ*, 763, 144
 Marinacci F. et al., 2018, *MNRAS*, 480, 5113
 Martig M., Bournaud F., Teyssier R., Dekel A., 2009, *ApJ*, 707, 250
 Matthee J., Schaye J., 2019, *MNRAS*, 484, 915
 Momcheva I. G. et al., 2015, *ApJS*, 225, 27
 Momcheva I. G. et al., 2016, *ApJS*, 225, 27
 Morselli L., Popesso P., Cibinel A., Oesch P. A., Montes M., Atek H., Illingworth G. D., Holden B., 2019, *A&A*, 626, A61
 Mosleh M., Hosseinnejad S., Hosseini-ShahiSavandi S. Z., Tacchella S., 2020, *ApJ*, 905, 170
 Moster B. P., Naab T., White S. D. M., 2013, *MNRAS*, 428, 3121
 Muzzin A., Marchesini D., van Dokkum P. G., Labbé I., Kriek M., Franx M., 2009, *ApJ*, 701, 1839
 Naiman J. P. et al., 2018, *MNRAS*, 477, 1206
 Nelson D. et al., 2018, *MNRAS*, 475, 624
 Nelson D. et al., 2019a, *Comput. Astrophys. Cosmol.*, 6, 2
 Nelson D. et al., 2019b, *MNRAS*, 490, 3234
 Nelson D., Genel S., Vogelsberger M., Springel V., Sijacki D., Torrey P., Hernquist L., 2015, *MNRAS*, 448, 59
 Nelson E. J. et al., 2012, *ApJ*, 747, L28
 Nelson E. J. et al., 2013, *ApJ*, 763, L16
 Nelson E. J. et al., 2016, *ApJ*, 828, 27
 Nelson E. J. et al., 2019c, *ApJ*, 870, 130
 Noeske K. G. et al., 2007, *ApJ*, 660, L43
 Oesch P. A. et al., 2018, *ApJS*, 237, 12
 Orr M. E. et al., 2017, *ApJ*, 849, L2
 Pacifici C., Oh S., Oh K., Lee J., Yi S. K., 2016, *ApJ*, 824, 45
 Papovich C. et al., 2015, *ApJ*, 803, 26
 Patel S. G. et al., 2013, *ApJ*, 766, 15
 Peng C. Y., Ho L. C., Impy C. D., Rix H.-W., 2002, *AJ*, 124, 266
 Pillepich A. et al., 2018, *MNRAS*, 473, 4077
 Pillepich A. et al., 2019, *MNRAS*, 490, 3196
 Pillepich A., Nelson D., Truong N., Weinberger R., Martin-Navarro I., Springel V., Faber S. M., Hernquist L., 2021, preprint([arXiv:2105.08062](https://arxiv.org/abs/2105.08062))
 Rodighiero G. et al., 2011, *ApJ*, 739, L40
 Salim S. et al., 2007, *ApJS*, 173, 267
 Schaye J. et al., 2015, *MNRAS*, 446, 521
 Schmidt K. B. et al., 2013, *MNRAS*, 432, 285
 Schreiber C. et al., 2015, *A&A*, 575, A74
 Semenov V. A., Kravtsov A. V., Gnedin N. Y., 2019, *ApJ*, 870, 79
 Sérsic J. L., 1968, Atlas de Galaxias Australes. Cordoba
 Shivaiei I. et al., 2015, *ApJ*, 815, 98
 Sijacki D., Springel V., Di Matteo T., Hernquist L., 2007, *MNRAS*, 380, 877
 Sijacki D., Vogelsberger M., Genel S., Springel V., Torrey P., Snyder G. F., Nelson D., Hernquist L., 2015, *MNRAS*, 452, 575
 Skelton R. E. et al., 2014, *ApJS*, 214, 24
 Somerville R. S., Davé R., 2015, *ARA&A*, 53, 51
 Sparre M. et al., 2015, *MNRAS*, 447, 3548
 Sparre M., Hayward C. C., Feldmann R., Faucher-Giguère C.-A., Muratov A. L., Kereš D., Hopkins P. F., 2017, *MNRAS*, 466, 88
 Sparre M., Springel V., 2016, *MNRAS*, 462, 2418
 Speagle J. S., 2020, *MNRAS*, 493, 3132
 Speagle J. S., Steinhardt C. L., Capak P. L., Silverman J. D., 2014, *ApJS*, 214, 15
 Springel V. et al., 2018, *MNRAS*, 475, 676
 Springel V., 2010, *MNRAS*, 401, 791
 Springel V., Di Matteo T., Hernquist L., 2005, *MNRAS*, 361, 776
 Springel V., Hernquist L., 2003, *MNRAS*, 339, 289
 Springel V., Pakmor R., Zier O., Reinecke M., 2020, *MNRAS*, 506, 2871
 Springel V., White S. D. M., Tormen G., Kauffmann G., 2001, *MNRAS*, 328, 726
 Starkeburg T. K., Tonnesen S., Koppenhafer C., 2019, *ApJ*, 874, L17
 Strateva I. et al., 2001, *AJ*, 122, 1861
 Suess K. A., Kriek M., Price S. H., Barro G., 2019, *ApJ*, 885, L22
 Szomoru D. et al., 2010, *ApJ*, 714, L244
 Tacchella S. et al., 2015a, *Science*, 348, 314
 Tacchella S. et al., 2015b, *ApJ*, 802, 101
 Tacchella S. et al., 2018, *ApJ*, 859, 56
 Tacchella S. et al., 2019, *MNRAS*, 487, 5416
 Tacchella S., Dekel A., Carollo C. M., Ceverino D., DeGraf C., Lapiner S., Mandelker N., Primack J. R., 2016b, *MNRAS*, 458, 242
 Tacchella S., Dekel A., Carollo C. M., Ceverino D., DeGraf C., Lapiner S., Mandelker N., Primack J. R., 2016a, *MNRAS*, 457, 2790
 Tacchella S., Forbes J. C., Caplar N., 2020, *MNRAS*, 497, 698
 Tal T. et al., 2014, *ApJ*, 789, 164
 Tasca L. A. M. et al., 2015, *A&A*, 581, A54
 Taylor E. N. et al., 2015, *MNRAS*, 446, 2144
 Terrazas B. A. et al., 2020, *MNRAS*, 493, 1888
 Thomas D., Greggio L., Bender R., 1999, *MNRAS*, 302, 537
 Tomczak A. R. et al., 2016, *ApJ*, 817, 118
 Torrey P., Vogelsberger M., Genel S., Sijacki D., Springel V., Hernquist L., 2014, *MNRAS*, 438, 1985
 Torrey P., Wellons S., Ma C.-P., Hopkins P. F., Vogelsberger M., 2017, *MNRAS*, 467, 4872
 Trager S. C., Somerville R. S., 2009, *MNRAS*, 395, 608
 van der Wel A. et al., 2014, *ApJ*, 788, 28
 van Dokkum P. G. et al., 2010, *ApJ*, 709, 1018
 van Dokkum P. G. et al., 2011, *ApJ*, 743, L15
 van Dokkum P. G. et al., 2013, *ApJ*, 771, L35
 van Dokkum P. G. et al., 2015, *ApJ*, 813, 23
 Vogelsberger M. et al., 2014a, *MNRAS*, 444, 1518
 Vogelsberger M. et al., 2014b, *Nature*, 509, 177
 Vulcani B. et al., 2015, *ApJ*, 814, 161
 Vulcani B. et al., 2016, *ApJ*, 833, 178
 Weinberger R. et al., 2017, *MNRAS*, 465, 3291
 Weinberger R. et al., 2018, *MNRAS*, 479, 4056
 Wellons S., Torrey P., 2017, *MNRAS*, 467, 3887
 Whitaker K. E. et al., 2011, *ApJ*, 735, 86
 Whitaker K. E. et al., 2014, *ApJ*, 795, 104
 Whitaker K. E. et al., 2019, *ApJS*, 244, 16
 Whitaker K. E., van Dokkum P. G., Brammer G., Franx M., 2012, *ApJ*, 754, L29
 Wuyts S. et al., 2011, *ApJ*, 742, 96
 Wuyts S. et al., 2012, *ApJ*, 753, 114
 Wuyts S. et al., 2013, *ApJ*, 779, 135
 Zibetti S., Charlot S., Rix H.-W., 2009, *MNRAS*, 400, 1181
 Zinger E. et al., 2020, *MNRAS*, 499, 768
 Zolotov A. et al., 2015, *MNRAS*, 450, 2327

APPENDIX A:

As noted in Section 3.3, in Fig. A2 we show the impact of orientation on average sSFR profiles across the SFMS. The primary region of parameter space where this turns out to be relevant is also the most

interesting: at high masses below the main sequence. Projection effects result in sSFR profiles that appear less centrally depressed than they are in reality if one could measure them face-on. This is relevant for our interpretation of observations.

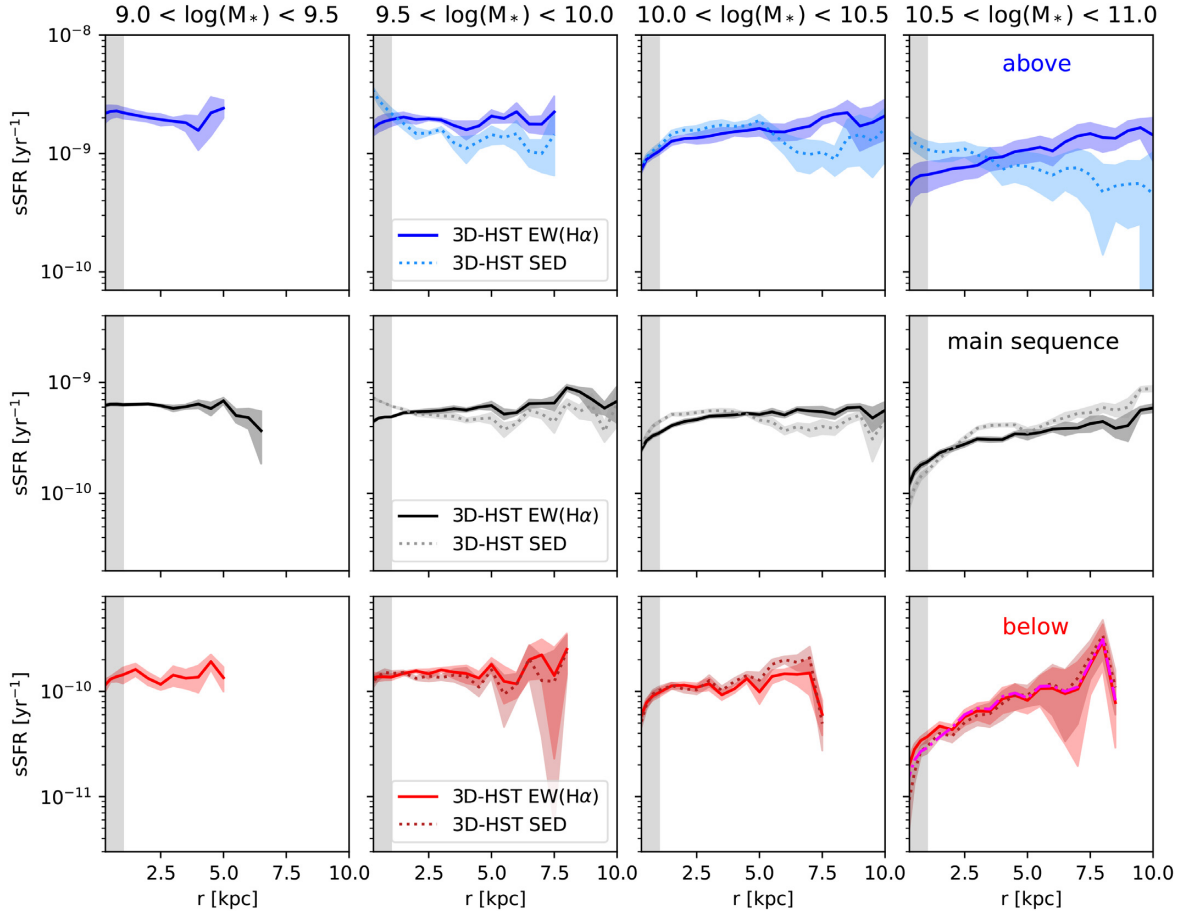


Figure A1. The average radial sSFR profiles of galaxies across the SFMS are very similar between TNG50 and observations at $0.75 < z < 1.5$. The top row is above the main sequence, middle is on, bottom is below. The magenta in the bottom right corresponds to the AGN correction described in Section 2.4, note it makes little difference. The grey shaded region is inside the observed PSF.

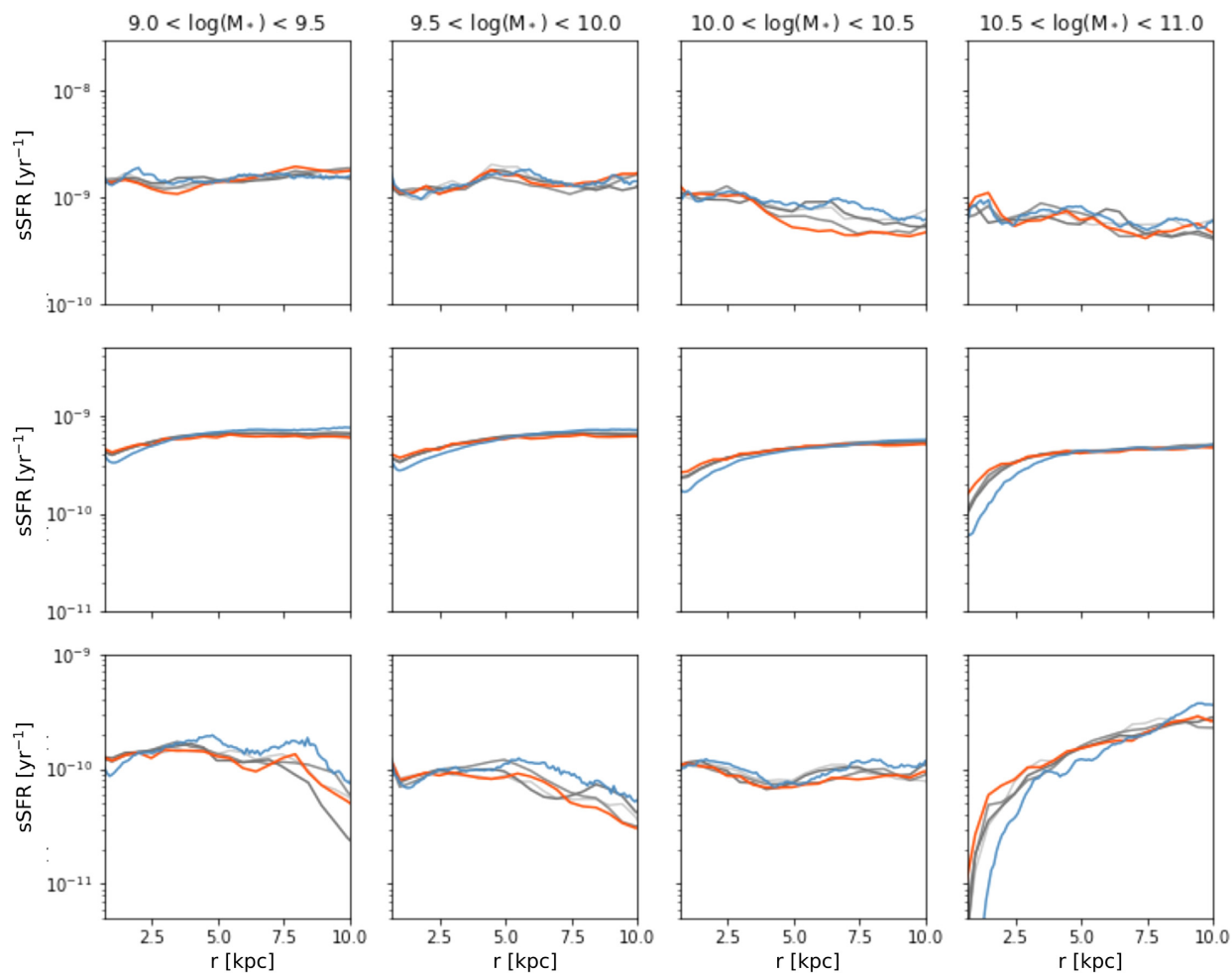


Figure A2. Here, we show the difference between sSFR profiles from TNG50 at different orientations. Blue is face on, orange is edge on, greys are xy , xz , and yz projections respectively. The top row is above the main sequence, the middle is on the main sequence, the bottom is below.

¹Department for Astrophysical and Planetary Science, University of Colorado, Boulder, CO 80309, USA

²Center for Astrophysics | Harvard-Smithsonian, Cambridge, MA 02138, USA

³Department of Astronomy, University of Maryland, College Park, MD 20742, USA

⁴Department of Astronomy & Astrophysics, The Pennsylvania State University, University Park, PA 16802, USA

⁵Institute for Computational & Data Sciences, The Pennsylvania State University, University Park, PA 16801, USA

⁶Institute for Gravitation and the Cosmos, The Pennsylvania State University, University Park, PA 16802, USA

⁷Department of Astronomy, University of Massachusetts, Amherst, MA 01003, USA

⁸Cosmic Dawn Center (DAWN), Copenhagen, 2200, Denmark

⁹Max-Planck-Institut für Astronomie, Königstuhl 17, D-69117 Heidelberg, Germany

¹⁰Institut für theoretische Astrophysik, Zentrum für Astronomie, Universität Heidelberg, Albert-Ueberle-Str 2, D-69120 Heidelberg, Germany

¹¹Niels Bohr Institute, University of Copenhagen, Jagtvej 128, København N DK-2200, Denmark

¹²Department of Physics and Astronomy, Rutgers University, 136 Frelinghuysen Rd, Piscataway, NJ 08854, USA

¹³Center for Computational Astrophysics, Flatiron Institute, 162 5th Avenue, New York, NY 10010, USA

¹⁴Astronomy Department, Yale University, New Haven, CT 06511, USA

¹⁵Department of Physics and Astronomy “Augusto Righi”, University of Bologna, via Gobetti 93/2, I-40129 Bologna, Italy

¹⁶Dunlap Institute for Astronomy & Astrophysics, University of Toronto, Toronto, ON M5S 3H4, Canada

¹⁷South African Astronomical Observatory, Cape Town 7935, South Africa

¹⁸Max-Planck-Institut für Astrophysik, D-85740 Garching bei München, Germany

¹⁹Department of Statistical Sciences, University of Toronto, Toronto, ON M5S 3G3, Canada

²⁰Department of Astronomy, University of Florida, Gainesville, FL 32611, USA

²¹Department of Physics and Kavli Institute for Astrophysics and Space Research, Massachusetts Institute of Technology, Cambridge, MA 02139, USA

²²Department of Physics, University of Bath, Claverton Down, Bath BA2 7AY, UK

This paper has been typeset from a $\text{\TeX}/\text{\LaTeX}$ file prepared by the author.